To the Graduate Council:

I am submitting herewith a thesis written by Jennie E. Cook entitled “Development of a Dilatant Damage Zone along a Thrust Relay in a Low-Porosity Quartz Arenite”. I have examined the final electronic copy of this thesis for form and content and recommend that it be accepted in partial fulfillment for the requirements for the degree of Master of Science, with a major in Geology.

William M. Dunne
Major Professor

We have read this thesis and
recommend its acceptance:

Robert D. Hatcher, Jr.

Linda C. Kah

Acceptance for the Council:

Anne Mayhew
Vice Chancellor and Dean of
Graduate Studies

(Original signatures are on file with official student records.)

Development of a Dilatant Damage Zone along a Thrust Relay in a Low-Porosity Quartz Arenite

A Thesis
Presented for the
Master of Science Degree
The University of Tennessee, Knoxville

Jennie E. Cook
December 2005

ACKNOWLEDGEMENTS

I would like to thank my advisor, Dr. Bill Dunne, for his guidance and patience, and for introducing me to quartz microstructures. He has been a mentor and friend whose unending support has made this project possible. I would also like to thank Dr. Charles Onasch for his help throughout the project including the use of his facilities at Bowling Green State University, help with fluid inclusion and FTIR analysis, and his expertise in the areas of quartz chemistry and the role of fluids in deformation. I am grateful to Dr. Linda Kah and Dr. Robert Hatcher, for the use of their facilities, guidance, and service on my thesis committee. I would also like to thank Dr. John Farver for his help with sample preparation and use of the scanning electron microscope at BGSU.

I would like to thank the NSF (Research Grant EAR-0087607), AAPG Grants-in-Aid-of-Research, and Southeast GSA for their financial support of this project. In addition, I am grateful to my field assistant, Janet Fitch, for her help carrying samples, step-ladders, and other field equipment up hills, through storms, and across rivers; and for assuring that I did not drown in the Potomac or fall from a cliff. Finally, I would like to thank all of my family and friends, without their support I could not have completed this project.

ABSTRACT

A damage zone developed along a backthrust fault system in well-cemented quartz arenite of the Tuscarora Sandstone in the Alleghanian foreland thrust system consists of a network of NW-dipping thrusts that are linked by multiple higher-order faults and bound a zone of intense extensional fractures and breccias. The damage zone is unusual in that it preserves porous brittle fabrics despite formation at >5km depth. The damage zone developed at an extensional step-over between two independent, laterally propagating backthrusts. Continued displacement resulted in breaching of the relay and formation of fault-bounded horses, and favored the formation of extensional fractures. The presence of pervasive, late-stage fault-normal joints in a fault-bounded horse in the northwestern damage zone indicates formation between two near-frictionless faults. This decrease in frictional resistance was likely a result of increased fluid pressure.

In addition to physical effects of fluid, chemical effects of fluid also influenced damage zone development. Quartz cements, fluid inclusion data, and FTIR analysis indicate that both aqueous and methane-dominated fluids were present within the damage zone. Although aqueous fluids are commonly present in the Tuscarora Sandstone, the presence of methane-saturated fluids is atypical. The backthrust network likely acted as a fluid conduit system, bringing methane-rich fluids up from the underlying Martinsburg Formation and displacing the resident aqueous fluids. The presence of methane was important for damage zone development in two ways. First, methane enhanced the effects of pore fluid pressure and facilitated brittle fracturing; and second, methane inhibited nucleation and precipitation of later-stage quartz cements, and thus the healing of later-stage fractures and breccias.

The cumulative effect of damage zone structures produced a zone of localized high porosity and permeability within a well-cemented quartz arenite at depth. The development and preservation of the dilatant damage zone results from (1) its formation at an extensional step-over, (2) lack of later-stage cementation, (3) and presence of locally elevated fluid pressures.

TABLE OF CONTENTS

Chapter	*Page*
1. INTRODUCTION	1
2. REGIONAL GEOLOGIC SETTING	3
3. DAMAGE ZONE	6
3.1 Mesoscale Structure	6
3.2 Microscale Structure	13
Microstructural Textures of Faults	13
Microstructural Textures of Horses	16
Microstructural Textures of Background Samples	19
Microstructural Abundances	19
4. FLUIDS WITHIN THE DAMAGE ZONE	23
4.1 Evidence for Fluids within the Damage Zone	23
4.2 Fluid Inclusion Microthermometry	23
4.3 Microscale Water Distribution from Fourier Transform Infrared Spectroscopy	26
5. DISCUSSION	29
5.1 Fluids in the Damage Zone	29
Source of Methane in the Damage Zone	29
5.2 Damage Zone Development	30
Evidence for Elevated Fluid Pressures During Damage Zone Development	30
Formation of an Extensional Relay in a Thrust System	32
6. CONCLUSIONS	35
REFERENCES CITED	36
APPENDICES	42
VITA	53

LIST OF TABLES

Table	*Page*
3.1 Joint intensity data	12
3.2 Microstructural abundances classified by primary deformation process	21
4.1 Fourier transform infrared spectroscopy (FTIR) data	28
A.1 Fault orientation data	45
A.2 Joint orientation data	46
A.3 Damage zone bedding orientation data	47
A.4 Chevron fold bedding orientation data	48
A.5 Microstructural abundances for the chevron fold classified by primary deformation process	49
A.6 FTIR data	50

LIST OF FIGURES

Figure	*Page*
2.1 Regional geology	4
2.2 Geologic map of the study area at Big Bend, WV	5
3.1 Cross section of the Cave Mountain anticline	7
3.2 Fieldsketch of the damage zone	8
3.3 Mesoscale structures within the damage zone	9
3.4 Fault and bedding orientation data from the damage zone	11
3.5 Mesoscale structures within the southeastern damage zone	11
3.6 Joint orientation data	12
3.7 Healed cataclasite and breccia	14
3.8 Partially cemented breccias	15
3.9 SEM images from porous breccia samples	17
3.10 Partially cemented breccias (cont.)	18
3.11 Photomicrograph of a background sample	20
4.1 Histogram of homogenization temperatures (T_h) for CH_4 inclusions	24
4.2 VX (molar volume/composition) diagram for CH_4 – CO_2 fluid inclusions	25
4.3 Water concentration from FTIR	28
5.1 Joints forming sub-normal to fault surfaces	31
5.2 Damage zone development	33
A.1 Locations of outcrop photos in Figs. 3.3, 3.5, and 5.1	43
A.2 Sample locations for the chevron fold	44

1. INTRODUCTION

Damage zones are deformed wall rock spatially associated with faults that form during the initiation and propagation of a fault, during the interaction of slip in fault linkages or jogs, or during the flexure of beds around a fault (Jamison and Stearns, 1982; Chester and Logan, 1986; Shipton and Cowie, 2001; 2003; Flodin and Aydin, 2004; Kim et al., 2004). An understanding of damage zones provides insight into faulting and displacement transfer processes, and the influence of fault structure on fault permeability (Antonelli and Aydin, 1994; Caine et al., 1996). Fault damage zones are broadly grouped into three categories based on their location relative to the host fault: tip damage zones that develop from stress perturbations at the fault tip; wall damage zones that develop because of slip accumulation, asperities, or tip damage zone abandonment; and linking damage zones that form by the interaction of slip between two linked faults (Kim et al., 2004; Tarasewicz et al., 2005). Damage zones have typically been described for near-surface strike-slip fault systems, some normal fault systems, and only a limited number of thrust faults (Chester and Logan, 1986; Shipton and Cowie, 2003; Flodin and Aydin, 2004; Kim et al., 2004). Although damage zones occur at all scales and in all lithologies, we concentrate on damage zone development within quartz-rich sandstone adjacent to a thrust fault system.

The development of faults and their associated damage zones in quartz-rich rocks, such as sandstone, are of particular interest because quartz-rich rocks are abundant in the upper crust (< 8 km) and quartz often serves as a proxy for upper crustal rocks in tectonic analyses. These fault zones are dominated by brittle deformation in the uppermost crust (<3 km depth) (Aydin, 1978; Antonelli and Aydin, 1994; Shipton and Cowie, 2003; Crider and Peacock, 2004). In this regime, two processes dominate fault and damage zone formation in porous sandstone (>20% porosity) (Davatzes and Aydin, 2003; Davatzes et al., 2005). The first process, deformation band development and faulting, involves the formation and localization of individual deformation bands, or tabular zones of cataclasis with small shear offsets into deformation band zones and discrete slip surfaces (Antonelli and Aydin, 1994; Shipton and Cowie, 2001; Flodin and Aydin, 2004). Through further localization, these slip surfaces may form a throughgoing fault surface that accommodates significant offset (Shipton and Cowie, 2001). The second process is sheared joint faulting, which involves the reactivation of pre-existing joints by shear. Joint reactivation also promotes the formation of secondary and higher order joints, and ultimately fault breccias (Myers and Aydin, 2004, Davatzes et al, 2005). Faults may develop both groups of structures by the continual addition of new deformation bands and fractures with slip accumulation (Crider and Peacock, 2004; Davatzes et al, 2005). In each group, deformation is dominated by brittle processes, including fracturing at grain-to-grain contacts, grain crushing and comminution, and grain rotation, attrition, and sliding (Antonelli and Aydin, 1994; Crider and Peacock, 2004; Kim et al, 2004).

With increasing depth in the upper crust (> 3 km depth), faulting processes change in quartz-rich sandstones because of a loss of original porosity and an increase in temperature and pressure (Houseknecht, 1988; Wu and Groshong, 1991, Lloyd and Knipe, 1992). The pretectonic porosity reduction from deeper burial and consequently increased compaction and cementation, reduces the number of grain-to-grain point loads, altering the grain-scale stress state and creating a more homogenous stress distribution between grains (Gallagher et al, 1974, Blenkinsop and Rutter, 1986). Consequently, fractures propagate along grain boundaries or nucleate from existing grain flaws rather than initiating at grain-to-grain contact points. Formation and subsequent linkage of these fractures localizes deformation, forming shear fractures and slip zones (Lloyd and Knipe, 1992). The transition in fracturing behavior with deeper burial (> 3 km depth) is complemented by a diversification of active deformation mechanisms including dislocation-related and solution-related processes favored by the greater pressure/temperature (P/T) conditions and increased in-situ and migrating fluids (Blenkinsop and Rutter, 1986; Wu and Groshong, 1991; Lloyd and Knipe, 1992). The abundance of these diagenetic and in-situ fluids, along with the prevalence of diffusion mass transfer may provide abundant quartz in solution to quickly heal joints and faults, which reduces or eliminates their local stress field perturbations and affects rock strength during subsequent deformation (Houseknecht, 1988; Lloyd and Knipe, 1992).

Fluid composition, particularly nonaqueous phases, may also alter the chemical behavior of fluid or possibly the physical behavior by blocking quartz diffusion pathways, inhibiting quartz cementation (Houseknecht and Spötl, 1993; Worden et al. 1998; Marchand et al., 2000; 2002; Haszeldine et al., 2003). As a result, stress perturbations from point loads and the presence of small voids may be more abundant. In such a case, deformation could be dominated by brittle mechanisms and resemble deformation in the uppermost crust (<3 km).

The purpose of this study is to investigate a dilatant damage zone located along a thrust fault. The damage zone is intriguing because it preserves porous fault breccias rather than healed cataclasite and has an intense, complex network of unhealed joints and secondary faults, despite being formed at depths greater than 5 km. Given the typical interplay of brittle-, dislocation- and solution-related processes in these conditions, the creation and preservation of this brittle-dominated rock volume and the relative lack of dislocation- and solution-related processes is unusual and has implications for the permeability of fault zones at depth. To understand the development of this zone, we characterize the deformation using detailed field sketches; microstructural abundances; plane, polarized, cathodoluminescence (CL), and scanning electron microscopy (SEM) imagery; fluid inclusion chemistry and microthermometry; and Fourier Transform Infrared (FTIR) spectroscopy.

2. REGIONAL GEOLOGICAL SETTING

The study area is located within the Alleghanian foreland thrust belt of the central Appalachians. Physiographically, the area lies within the Valley and Ridge Province, which is bordered to the west by the Appalachian structural front and to the east by the Blue Ridge Province (Fig. 2.1). The rocks of the Valley and Ridge Province are Paleozoic, consisting of a roof sequence of middle Ordovician to Pennsylvanian, dominantly clastic rocks, overlying Cambrian to middle Ordovician carbonates in the Alleghanian duplexes that rest on autochthonous Cambrian rocks (Perry, 1978; Hatcher et al., 1989). The study area exposes Silurian Tuscarora Sandstone in the hinge of the Cave Mountain anticline along meanders of the South Branch of the Potomac River (Fig. 2.2) (Sites, 1971; Gerritsen, 1988). The Cave Mountain anticline is a first-order, mapscale, asymmetric, doubly plunging anticline located directly to the east of the Wills Mountain anticlinorium and overlies a culmination in the underlying duplex of Cambro-Ordovician rocks (e.g. Wilson and Shumaker, 1992).

This study was limited to the early Silurian Tuscarora Sandstone, a clean, white, silica-cemented quartz arenite. The Tuscarora Sandstone is a framework-supported, medium grained sandstone, typically containing less than 3% porosity, although some zones of slightly higher porosity may locally be present (Sibley and Blatt, 1976; Cotter, 1983; Houseknecht, 1988; Dorsch and Driese, 1995; Diecchio and Dennison, 1996). In the central Appalachians, the Tuscarora Sandstone experienced a maximum burial of approximately 6 km. Based on both conodont color alteration indices and burial depth, the Tuscarora was deformed during the Alleghanian Orogeny at temperatures between 150º-200º C (Harris et al., 1977; Onasch and Dunne, 1993). Although the Tuscarora Sandstone can have a thickness of up to 150 m, the thickness is 75 m at the study location (Reger and Tucker, 1924). Here the unit contains a stratigraphic marker package: a prominent shale layer, about 3 m thick, located approximately in the center of the unit that is overlain by a bioturbated, clay-rich sandstone with a distinctive outcrop appearance.

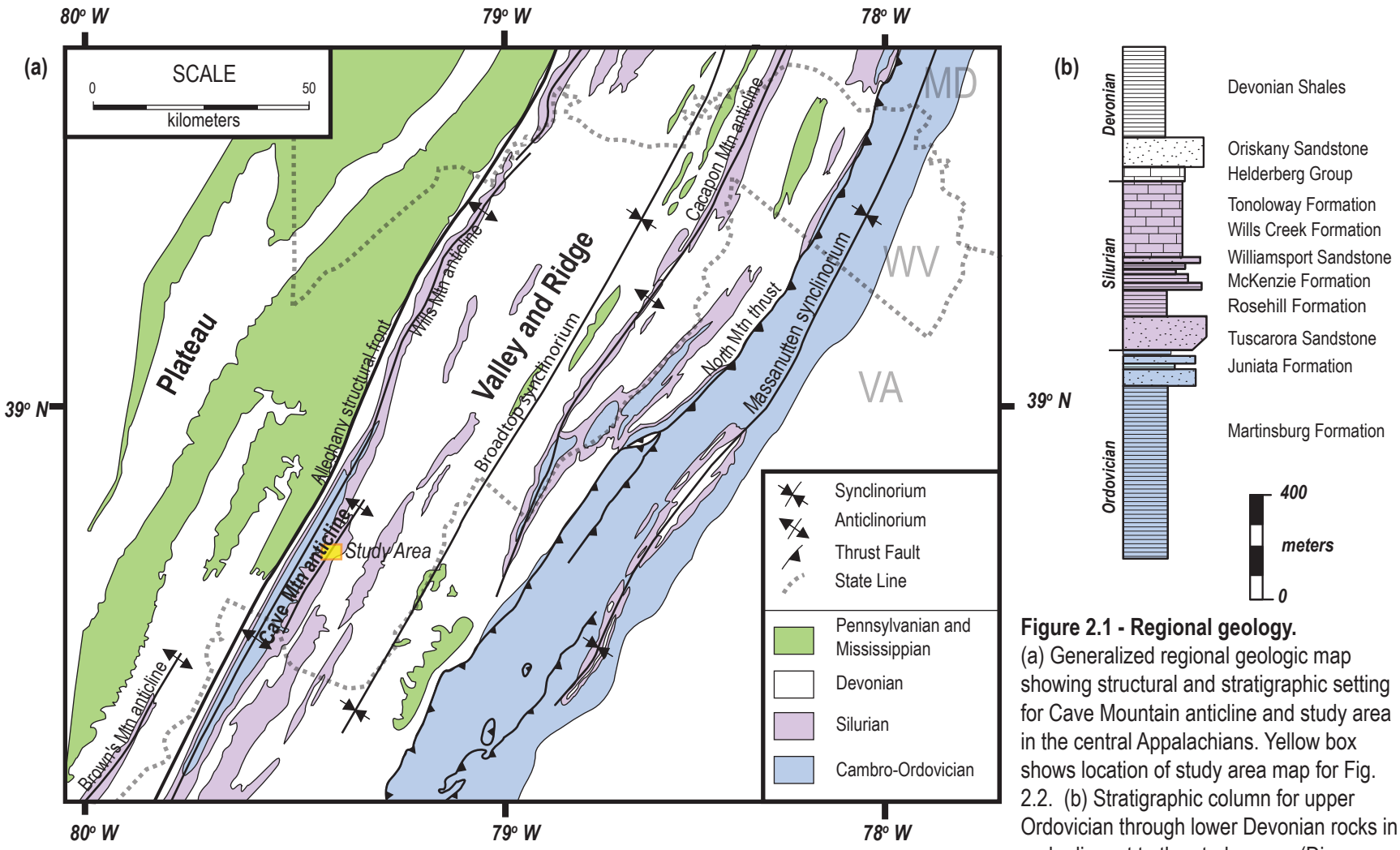


Figure 2.1 - Regional geology.
(a) Generalized regional geologic map showing structural and stratigraphic setting for Cave Mountain anticline and study area in the central Appalachians. Yellow box shows location of study area map for Fig. 2.2. (b) Stratigraphic column for upper Ordovician through lower Devonian rocks in and adjacent to the study area. (Diagrams modified from Dunne, 1996)

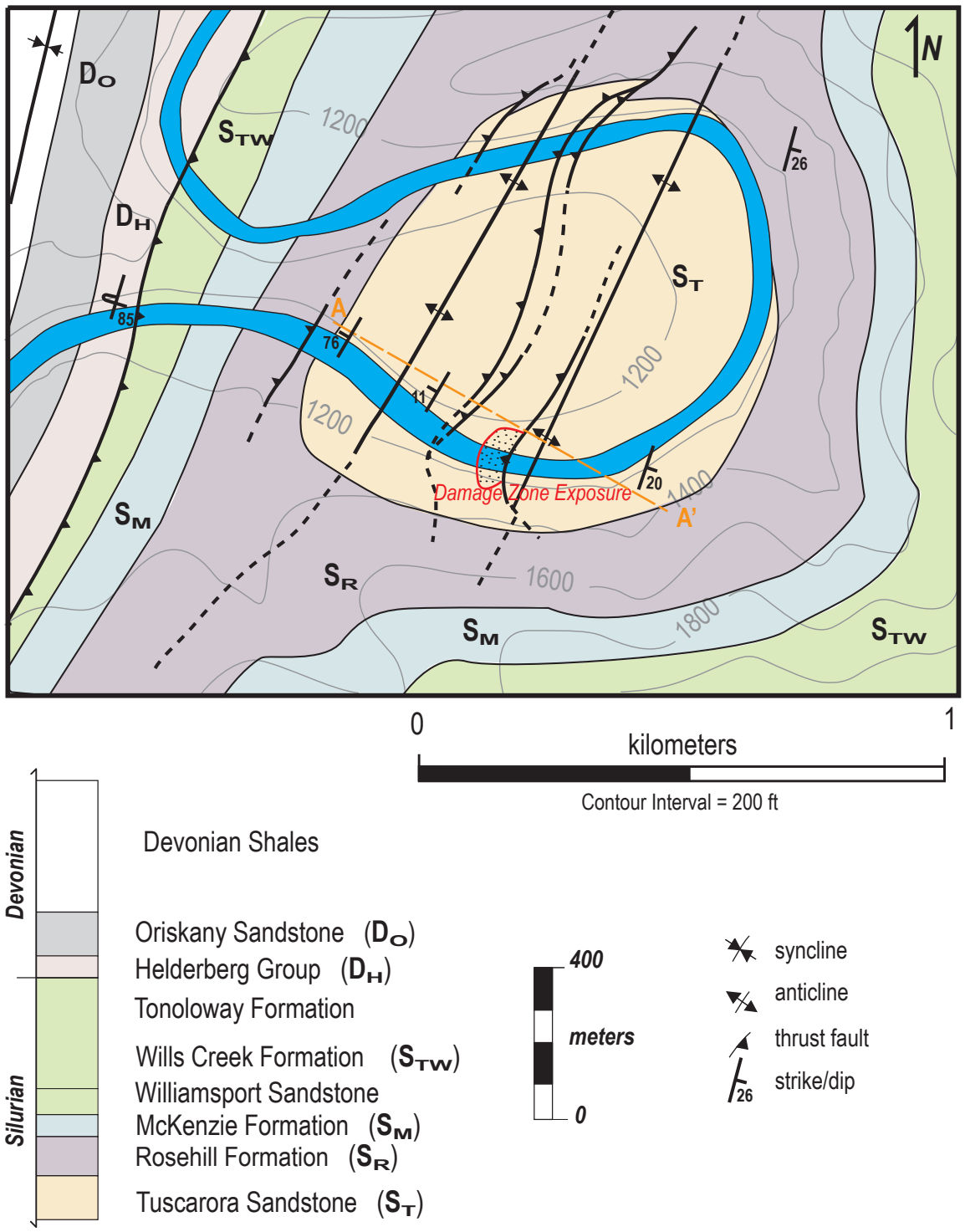


Figure 2.2 - Geologic map of the study area at Big Bend, WV. Map shows traces of subhinges, faults, and the lower Paleozoic stratigraphy exposed in the culmination of the Cave Mountain anticline. The damage zone is exposed along the southeasternmost backthrust in both banks of the South Branch of the Potomac River (dark blue). Section A-A' for cross section in Fig. 3.1 (adapted from Gerritsen, 1988).

3. DAMAGE ZONE

The asymmetric, northwest-vergent geometry of the Cave Mountain anticline at its culmination is achieved by a gradual dip change from shallow southeast to sub-horizontal at a broad, open hinge, and from sub-horizontal beds to steeply northwest and overturned bed dips at a chevron-style hinge (Fig. 3.1). At this parasitic hinge, the shale layer of the Tuscarora Sandstone is locally thickened within the NW end of the study area (Fig. 3.1). The anticlinal culmination contains three backthrusts and two smaller fold hinges within the study area (Figs. 2.2, 3.1). These backthrusts have less than 30 m displacement and are interpreted to link with a larger, northwest-vergent thrust fault at depth. Northeast along strike approximately 500 m, the backthrust system becomes larger with total displacement exceeding 50 m. These faults contributed significantly to shortening within the study area but are rare elsewhere (Dunne, 1996) and their occurrence is most likely a function of their location at the anticlinal apex.

The damage zone is located along the most southeasternmost backthrust exposed in the hinge region, and is the only fault associated with such a feature. Although intense deformation has been investigated elsewhere in the Tuscarora Sandstone (e.g. Narahara and Wiltschko, 1986; Dransfield and Groshong, 1988; Couzens et al., 1993; Onasch and Dunne, 1993; Couzens and Dunne, 1994; Thorbjornsen and Dunne, 1997; Harrison and Onasch, 1999; Osborne et al., 2003) the existence of a damage zone has not been previously identified.

3.1 Mesoscale Structure

The damage zone is located at an extensional step-over along the backthrust that transfers displacement from the northwest to the southeast (Figs. 3.1, 3.2) (Walsh et. al, 1999; Ferrill and Morris, 2001). The zone has a strike-normal length of approximately 30 m, and is at least 100 m wide along strike, and is exposed along both banks of the South Branch of the Potomac River (Fig. 2.2). The damage zone consists of a network of linking faults, secondary to the main backthrust, which bound intense zones of joints, smaller linking faults, and zones of fault rocks including porous fault breccias. Based on measurements on offset bedding surfaces from exposed faces on both riverbanks, the host fault has < 10 m of cumulative displacement (Fig. 3.2).

Secondary faults are discrete slip surfaces, often with kinematic trend indicators such as slickensides. Higher-order slip surfaces branch and link from these second-order surfaces (Figs. 3.3a, b). The most well developed breccia zones are typically found in the footwall of the second-order fault surfaces, and often in the zone bounded by the second-order slip surface and the branch point for a higher order splay fault (Figs. 3.2, 3.3c). These fault rocks and breccias are loosely consolidated in hand specimen and typically lack cement. The breccias consist of larger clasts in a matrix of smaller clast fragments and grains.

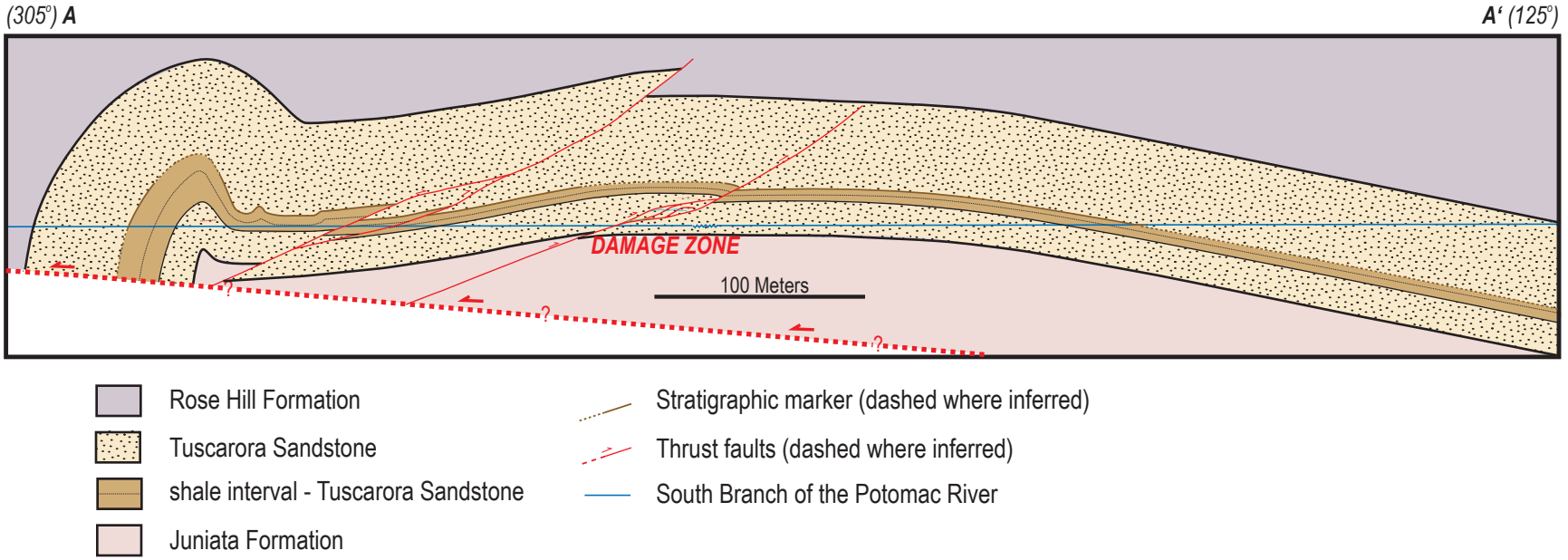
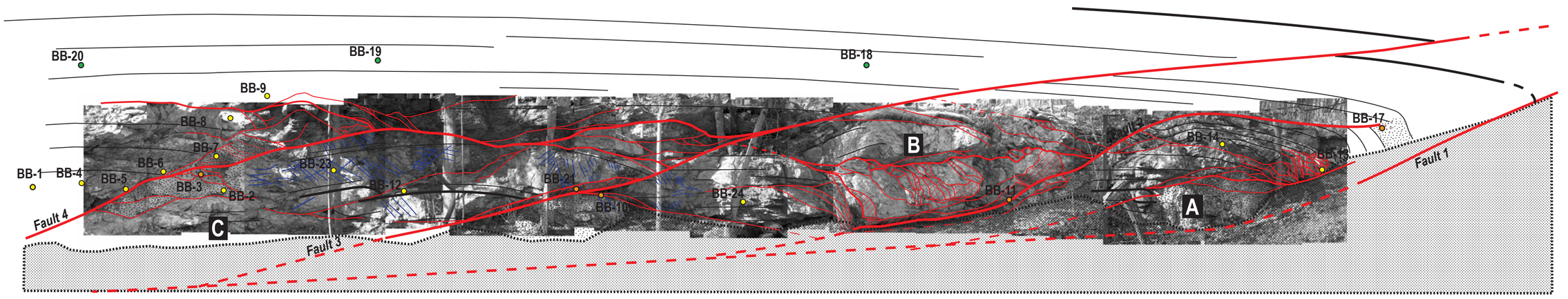


Figure 3.1 - Cross section of the Cave Mountain anticline. Section line A-A' across Cave Mountain anticlinal culmination (location in Fig. 2.2). Northwest portion of profile is based on data from the northeast bank of the South Branch of the Potomac River, while southeast portion is based on data from the southwest bank.

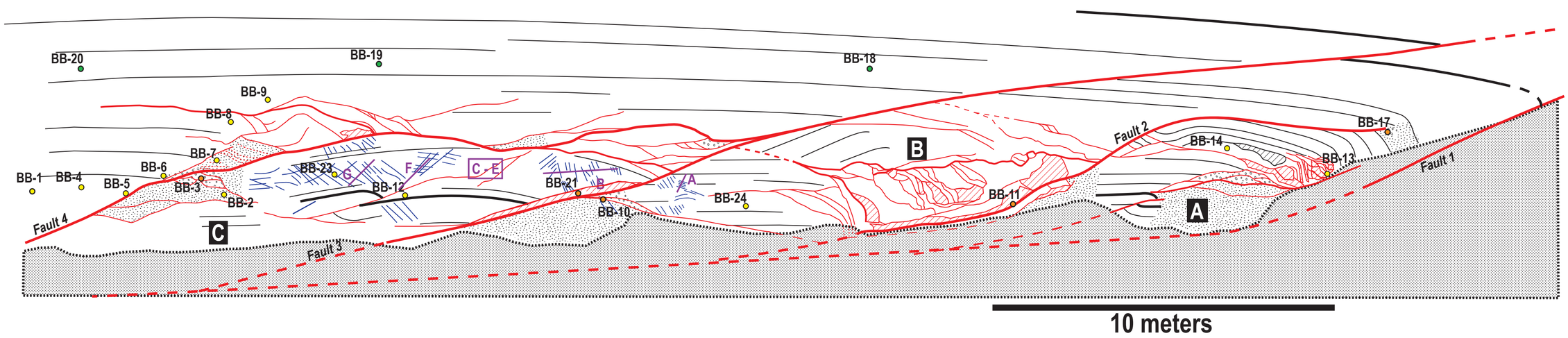
(a)



(b)



(c)



(d)

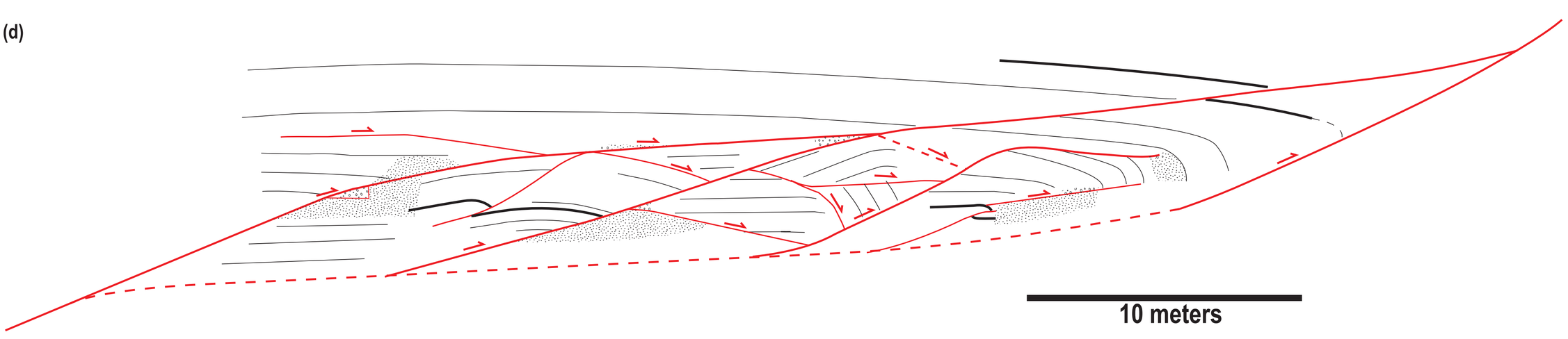
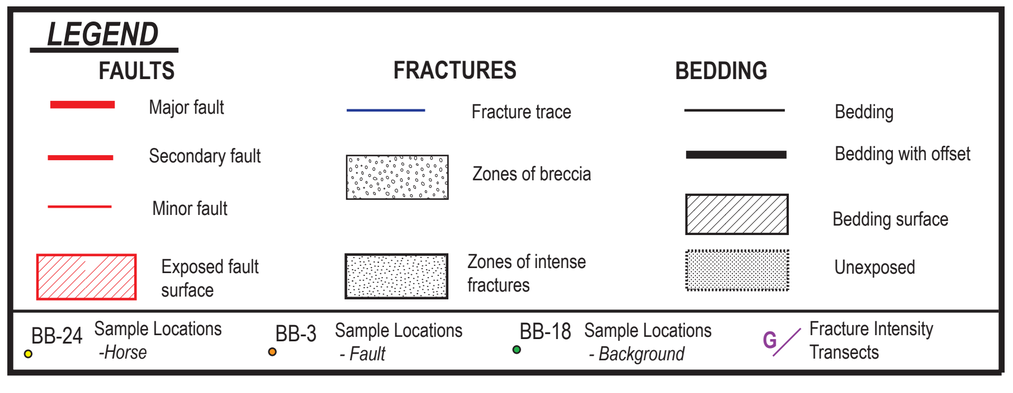


Figure 3.2 - Field sketch of the damage zone. (a) Photomosaic of the damage zone exposure; (b) Photomosaic with field sketch overlay; (c) Detailed field sketch showing major features of the exposure, numbered faults, fault-bounded packages A - C, fracture intensity transects, and sample locations; (d) Schematic diagram of the damage zone with major faults and interpreted bedding relationships. Location of exposure is 38.8885° N, 79.2418° W.



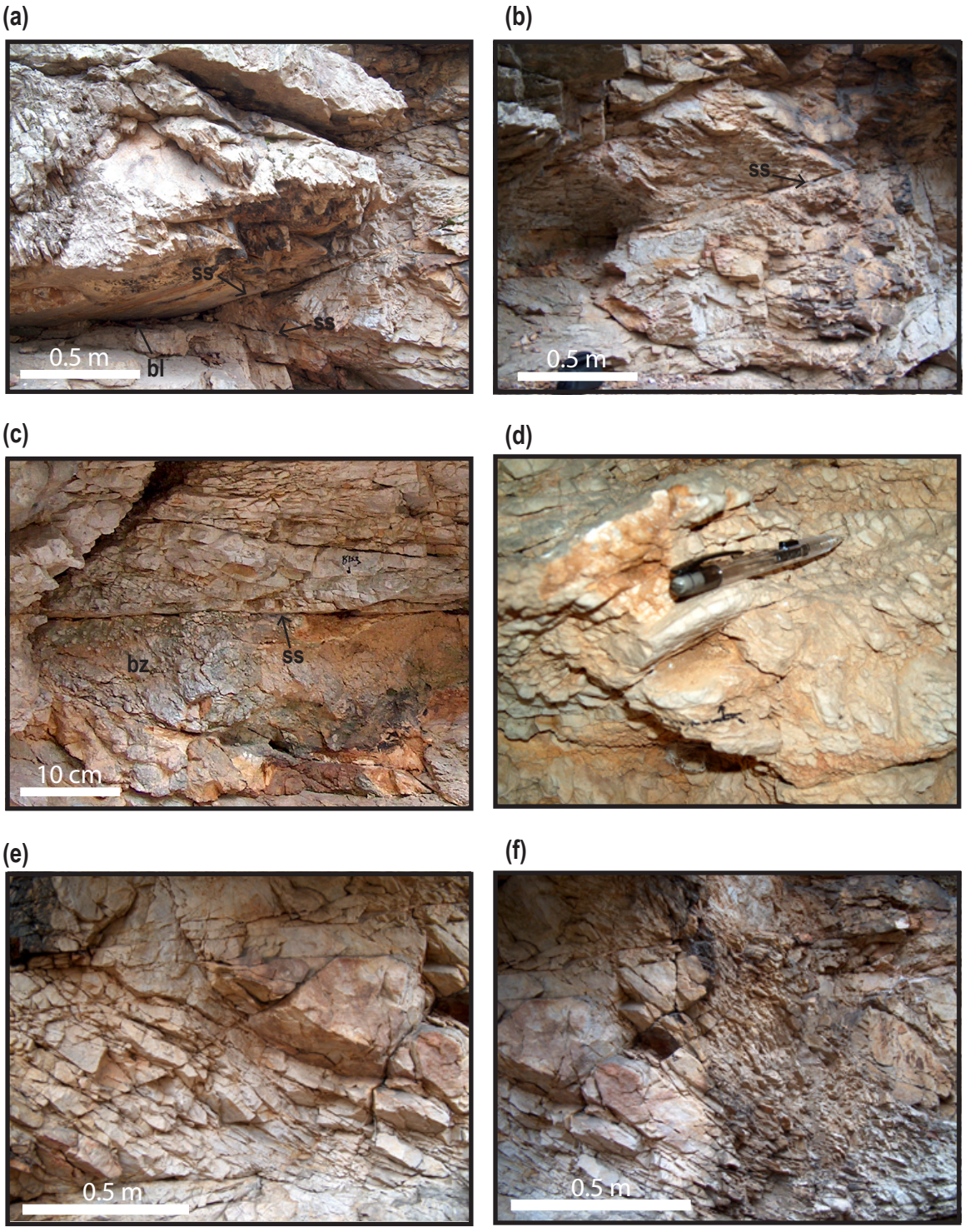


Figure 3.3 - Mesoscale structures within the damage zone. (a) Second-order slip surface (ss) and branch line (bl) with minor fault surface; (b) Slip surface (ss) surrounded by well-developed breccias and intensely fractured wall rock; (c) Breccia zone (bz) and associated slip surface (ss); (d) Breccia zone with narrow breccia seams and relatively larger clast sizes; (e) and (f) Overlapping photos of intensely jointed wall rock.

The breccia zones transition to weakly brecciated rocks where clast size is large and breccia seams are narrow (Fig. 3.3d), and then to intensely fractured rocks where breccia is absent (Figs. 3.3e, f).

Faults within the damage zone strike NE–SW and are dominantly dip-slip (Figs. 3.4a, b). The damage zone contains four faults that are second-order to the host backthrust. Three are exposed along the NE bank, and a fourth is unexposed, but is detectable based on bedding offsets in the SW bank. For the purposes of this paper, second-order faults are numbered 1 through 4, from the southeast and to the northwest, and the horses bounded by these faults are A to C, respectively (Fig. 3.2).

Bedding to fault geometry, accumulated fault slip, and internal structure of the horses change across the damage zone. Bedding rollover occurs adjacent to faults 1 and 2, producing an anticline above the damage zone (Figs. 3.2, 3.4c). The beds truncated by faults 3 and 4, however, only have a slight curvature into the faults.

Fractures are pervasive throughout the damage zone, but the geometry and intensity changes between horses. Within horses A and B, bedding is typically recognizable. Joints are infrequent and non-systematic, but are locally intense at bedding rollovers (Fig. 3.5a) and near fault 3. Small-scale faults along bedding are prevalent at bedding rollovers (Fig. 3.5b). In contrast, away from fault branch points in horse C, the rock is pervasively fractured but lacks fault breccia or kinematic indicators, thus these fractures are interpreted to be joints (Figs. 3.3e, f). Joint-bounded wall rock within this zone has little or no outcrop-scale evidence of veins, stylolites, or breccias. Joint intensities within this zone are typically between 15 to 80 m^{-1} (Table 3.1), much greater than typical intensities of 0.5 to 4 m^{-1} for most rocks with joints (Rohrbaugh et al., 2002). Joint orientations vary within horse C, but three dominant groups are recognized: (1) strike-parallel to the second- and higher-order faults; (2) striking north-northwest dipping 30º to 70º to the northeast; and (3) striking north-northwest dipping 60º to 80º to the southwest (Fig. 3.6). Joints within group (1) have a girdle distribution where the girdle is parallel to the girdle of fault orientations, consistent for secondary fractures related to slip on a fault, and are therefore interpreted to be related to slip along faults 3 and 4. Groups (2) and (3) have polar distributions and have similar strikes but dip directions are opposite with acute bisectrix angle of 60º to 90º. The strike orientation of these fractures is oblique to fault strike and transport directions and may indicate formation within a three-dimensional strain field during damage zone formation (Ismat and Mitra, 2001).

Most classification schemes for damage zones are based on strike-slip fault systems. Many authors agree, however, that these classifications can include thrust and normal fault systems (Woodcock and Fischer, 1986; Sibson, 1987; Walsh et al., 1999; Kim et al., 2004). Of the three main damage zone types: tip, wall, and linking, this damage zone morphologically resembles a linking damage zone, more specifically an extensional step-over. These damage zones evolve as a relay between two interacting fault

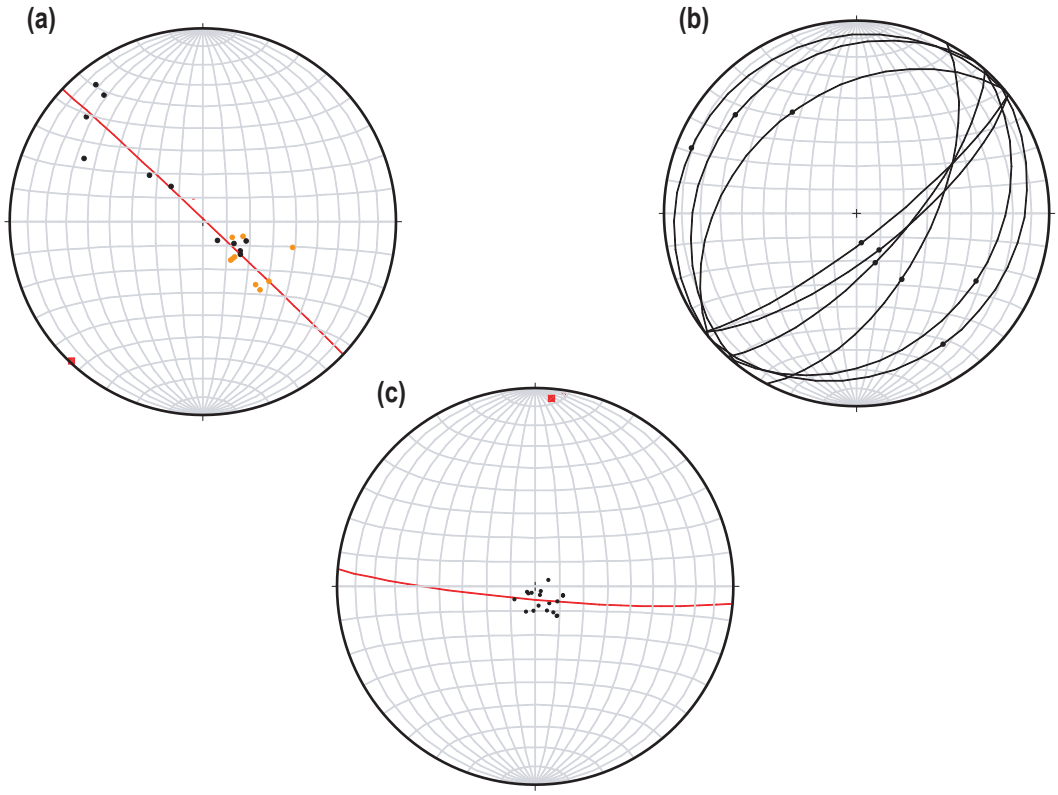


Figure 3.4 - Fault and bedding orientation data from the damage zone. (a) Poles of fault planes in lower hemisphere, equal-area stereonets. Poles to second-order faults are orange, higher-order surfaces are black. Red square represents best-fit fault trend of 043^{o} - 223^{o}. (b) Great circles for faults with trends (black points) of slickensides indicating that fault motion is dominantly dip-slip. (c) Poles to planes for bedding surfaces associated with fault rollover at the southeastern edge of the damage zone exposure. Red square represents best-fit fold axis, generally trending north with a slight northeast plunge.

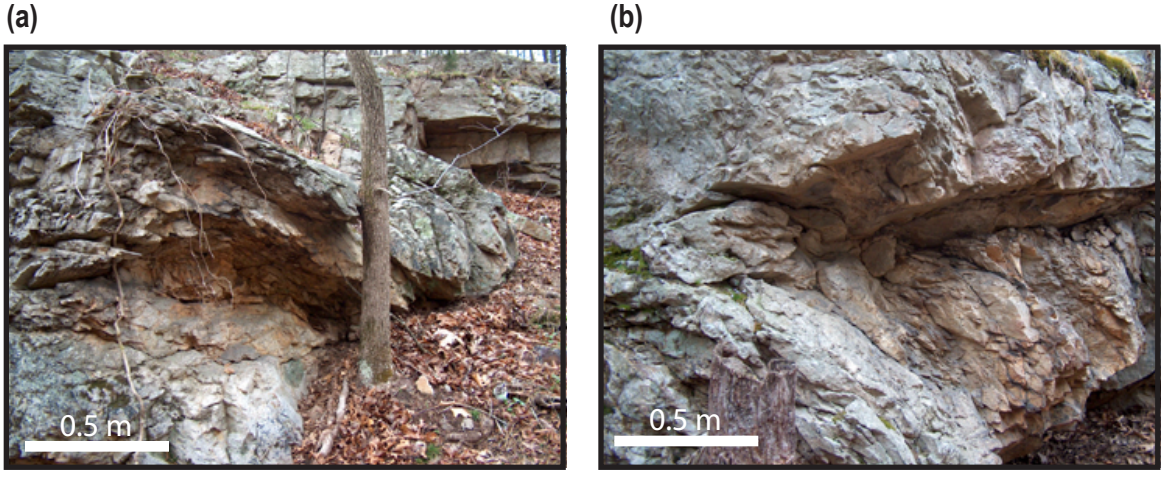


Figure 3.5 - Mesoscale structures within the southeastern damage zone. (a) Localized, systematic fractures associated with bedding rollover at southeastern end of damage zone adjacent to fault 1 (Fig. 3.2). (b) Faults and non-systematic fractures associated with bedding rollover along Fault 2.

Table 3.1 - Joint intensity data. Transects are shown in Fig. 3.2.

Transect	Intensity	Joint Orientations	
A	80 m-1	010/20 E	018/23 E
B	47 m-1	163/73 E	172/78 E
C	16 m-1	142/67 SW	136/70 SW
D	22 m-1	120/14 SW	100/10 SW
E	18 m-1	152/68 W	
F	84 m-1	138/32 NE	155/35 NE
G	41 m-1	125/38 NE	147/42 NE

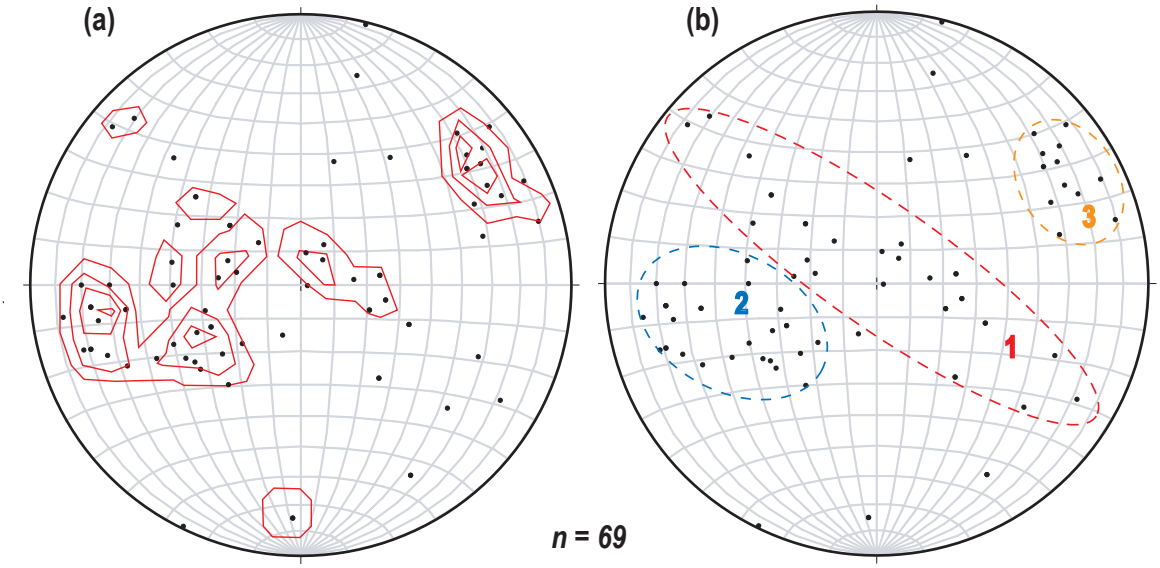


Figure 3.6 - Joint orientation data. (a) 1% area contour of poles to joints in lower-hemisphere, equal-area stereonets from the damage zone. Contour interval is 2% per 1% area. (b) Stereonet of poles to joints from the damage zone. Joint orientations are in three groups recognized from 1% area plot. Poles to joints in group 2 have a vector mean orientation of 255/43; and group 3 poles have a vector mean orientation of 62/20.

tips and typically exhibit intense fracturing when compared with other types of damage zones (Kim et al., 2004). Other extensional step-overs contain joints formed parallel to the local maximum principal stress directions (Sibson, 1987; Ohlmacher and Aydin 1997; Kim et al., 2004) and rotated blocks (Kim et al, 2004). Within the Cave Mountain damage zone, although grain rotation occurs within the breccia, large-scale block rotation is absent. Intense, mesoscale joints, however, are present. Fractures do accommodate fault-parallel extension, but the varied fracture orientation indicates that other mechanisms of fracture formation were active as well.

3.2 Microscale Structure

To investigate the interplay between brittle, dislocation-related, and solution-related deformation within the damage zone, 21 oriented samples were collected from rock adjacent to fault surfaces, internal horses within the damage zone, and background samples adjacent to and above the damage zone. Each thin section was examined using plane (PL), cross-polarized (CPL) and cathodoluminescence (CL) microscopy and some porous breccia samples were examined using scanning electron microscopy (SEM). CL was used to investigate microstructural relationships such as relative abundance of cement versus detrital grains, grain-to-grain relationships, and the presence of fracture fills (Onasch, 1990; 1995; Onasch and Dunne, 1993). CL aids in the interpretation of such features because silica cements and fracture fills typically grow in optical continuity with host rock grains, making these features difficult to identify under PL or CPL, but such features typically differ in luminescent properties (Sprunt and Nur, 1979; Blenkinsop and Rutter, 1986; Onasch, 1990; Laubach, 2003).

Microstructural Textures of Faults

Samples from second-order faults typically contain two end-member morphologies: (1) healed breccia and cataclasite with little to no porosity (Fig. 3.7); and (2) breccias with partially cemented porosity (Fig. 3.8). For the first morphology, fault textures include cemented breccia and cataclasite, abundant microveins, and fluid-inclusion planes. Breccia and cataclasite zones are often linear and narrow, except with proximity to the host fault. Linear breccia/cataclasite zones typically have offsets of few to several millimeters. Microveins occur as anastamosing nests and zones, or as linear features. For example, in sample BB-11 along fault 2, microveins and fluid-inclusion planes overprint cataclasite and healed breccias, indicating that this fault ceased movement prior to formation of filled fractures (Fig. 3.7a). In contrast, sample BB-21 along fault 3, has abundant cataclasite, which could indicate multiple periods of movement.

Porous, partially cemented, fault breccias are characterized by large, relatively undeformed clasts in a matrix of smaller, brecciated clasts and grains (Figs. 3.8a, b). All samples contain partial cement with

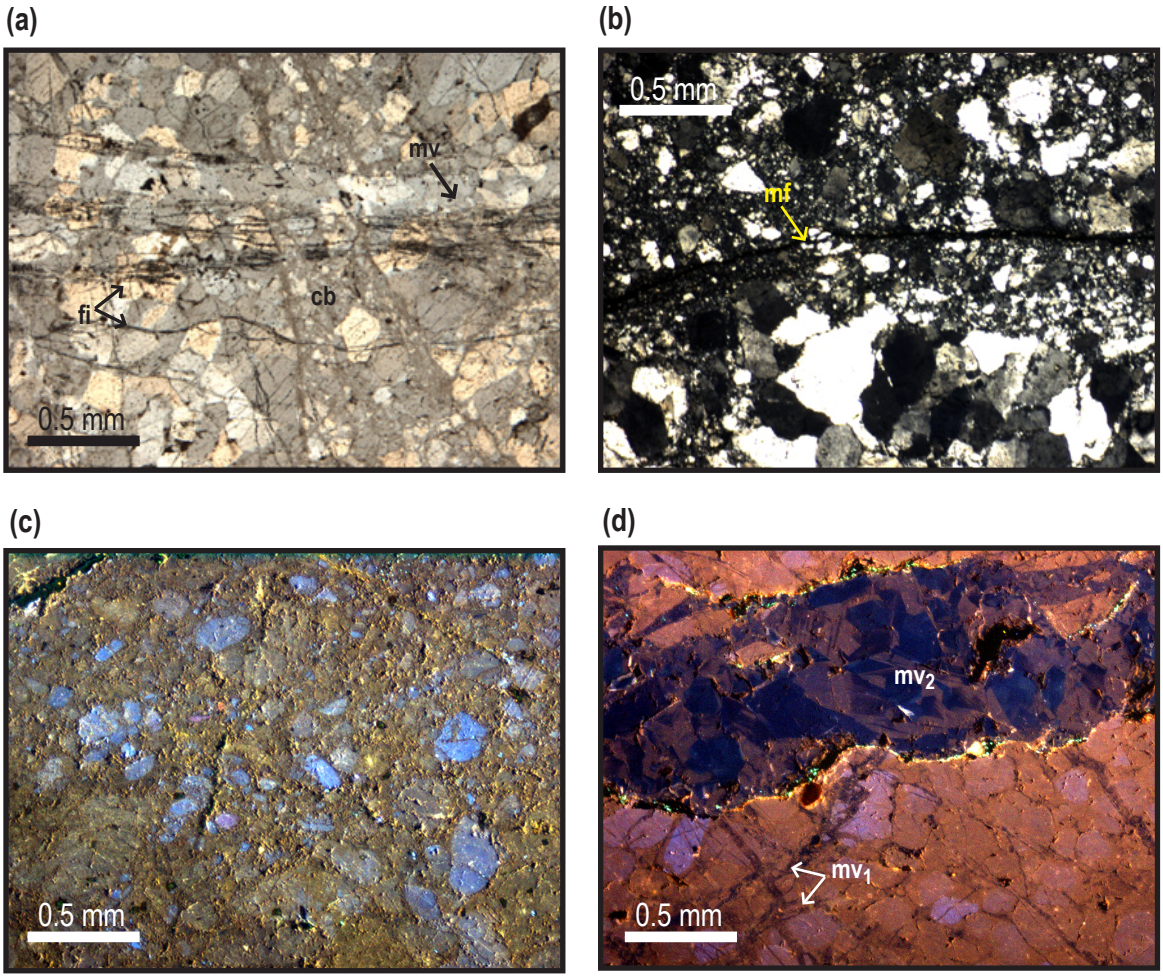


Figure 3.7 - Healed cataclasite and breccia. (a) CPL image of a cataclastic band (cb) crosscut by later coeval microveins (mv) and fluid inclusion planes (fi) (BB-11). (b) CPL image of a healed cataclasite zone surrounding a discrete slip surface (mf) (BB-21). (c) CL image of healed breccia (BB-21). (d) CL image of earlier microveins (mv_1) crosscut by later, larger microvein (mv_2) that is not completely healed. Solution has occurred along the edges of the later microvein (BB-11).

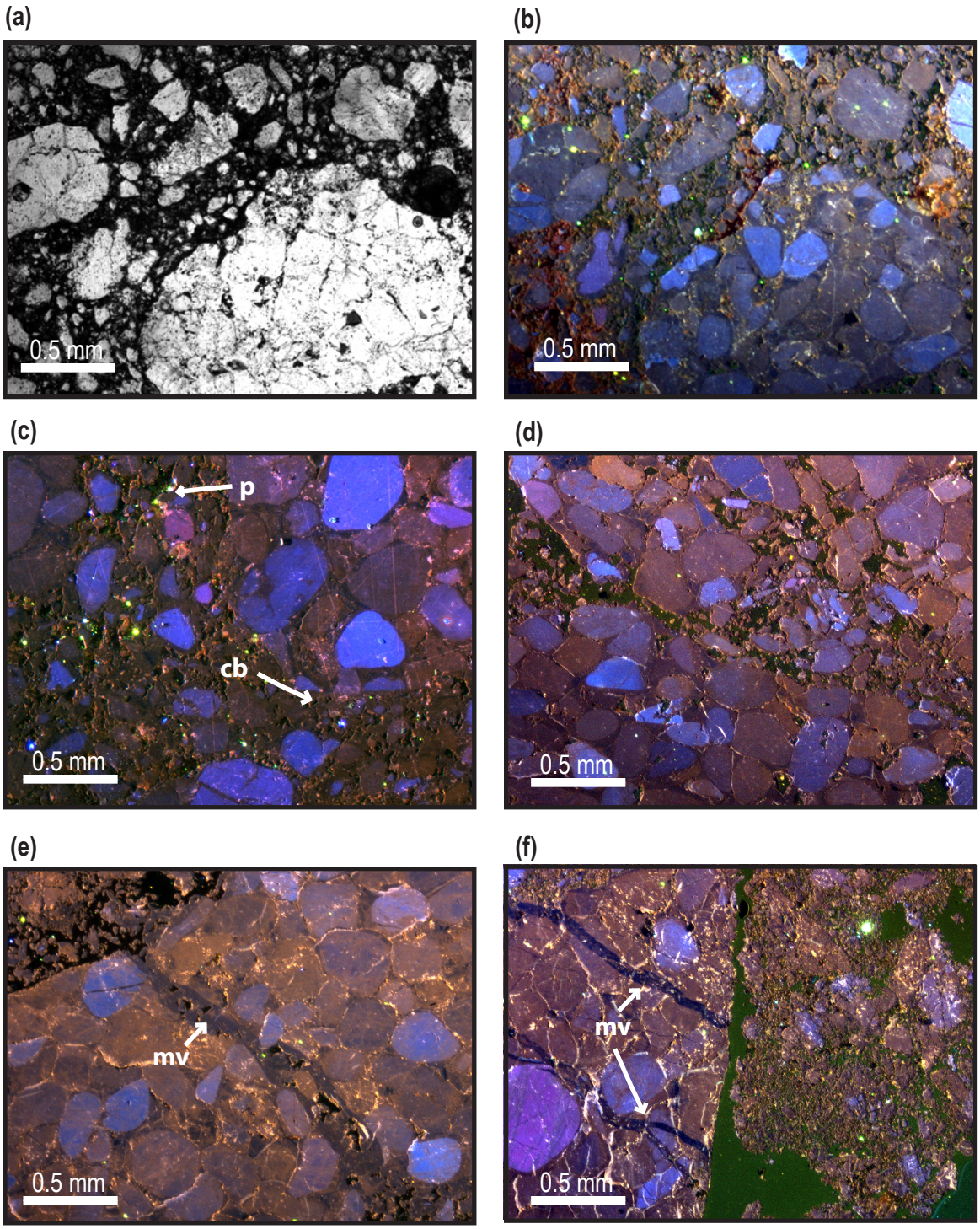


Figure 3.8 - Partially cemented breccias. In CL images, open porosity typically appears dark grey or green, while fracture fills and late-stage cements appear dark purple or blue. (a) PL and (b) CL images of larger cataclasts surrounded by intense breccia zones (BB-3). (c) CL image of partially healed breccia with open porosity (p) and cement bridges (cb) (BB-3). (d) CL image of relatively narrow breccia seam surrounded by host rock (BB-6). (e) CL image of a partially cemented microvein intersecting a breccia zone (BB-10). (f) CL image of earlier microveins (mv) truncated by partially healed breccia zone (BB-10).

abundant secondary porosity (Figs. 3.8b, c, d, e, f). Clast size increases and matrix abundance decreases with greater distance from the faults (Fig. 3.8d). Partially cemented fault breccias differ from healed fault breccias. Porosity is greater, breccia zones are widespread and typically non-linear, and large clasts may be sub-rounded, rather than angular, indicating greater rotation.

In most breccia samples, completely or partially cemented microveins (Fig. 3.8e), healed grain fragments, and fluid-inclusion planes are overprinted by breccia (Fig. 3.8f). Healed structures are interpreted to predate breccia formation because most microveins do not cut multiple breccia clasts and fluid-inclusion planes have different orientations in adjacent cataclasts. Partial cement in breccia samples occurs locally between clasts and matrix, between clasts, and along fracture walls of microfractures. In both cases, euhedral crystals partially infill the void space (Fig. 3.9a). Another texture consists of cataclasts "floating" in cement, where again, pores are common (Fig. 3.8c). Breccia samples BB-3 and BB-10 contain cement fragments, little cement between cataclasts, iron-oxide infills (Fig. 3.9b), and abundant porosity, supporting the interpretation that the breccia-forming displacement fractured pre-existing, partially cemented fault rocks. (Figs. 3.10a, b). Both breccia samples contain multiple breccia morphologies (Fig. 3.10b), corresponding to multiple breccia-forming fault displacements.

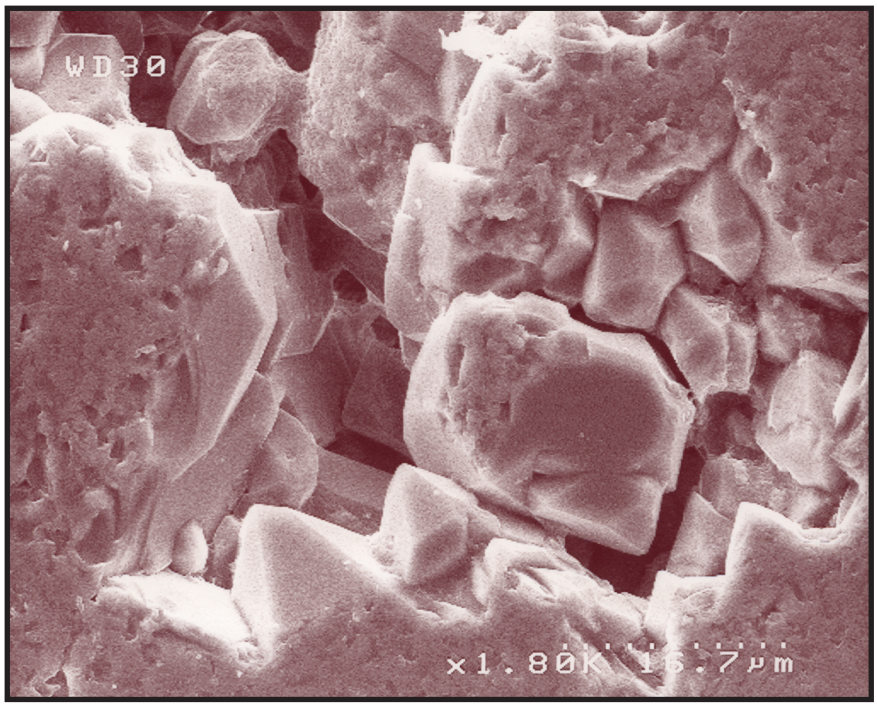
Pressure solution features such as stylolites are rare but occur in both groups of fault samples and typically occur in zones with greater clay contents. Stylolites are often cut by cataclasite, breccia, and microveins, but may cut across these structures (Fig. 3.10c). Stylolites likely formed early, but were active through much of damage zone development. Exceptions include stylolites formed within breccia zones of samples BB-3 and BB-10. Within these samples, stylolites are locally developed between cataclasts, and along unhealed voids and fractures (Fig.3.10d). These structures must have formed during late brecciation or after brecciation, as both would preserve stylolites.

Zones of localized breccia and grain disaggregation may provide insight into the formation of larger breccia zones. For example, breccia within the host rock preferentially forms at shear fracture intersections or overlaps (Fig. 3.10e). Because such zones remained open, they would have localized further deformation resulting in the accumulation of fragmentation and rotation at a larger scale.

Microstructural Textures of Horses

Samples from horses rarely contain breccias, disaggregated zones, or cataclastic fabrics except in bedding rollovers and intensely fractured zones. Horse samples typically contain healed and unhealed fractures manifested as fluid-inclusion planes and joints, respectively. Pressure solution features are rare and likely formed early. Locally, however, horse samples contain diverse structural suites. For example, BB-13 from bedding rollover contains localized cataclastic textures, microveins, and microfaults related to fold

(a)



(b)

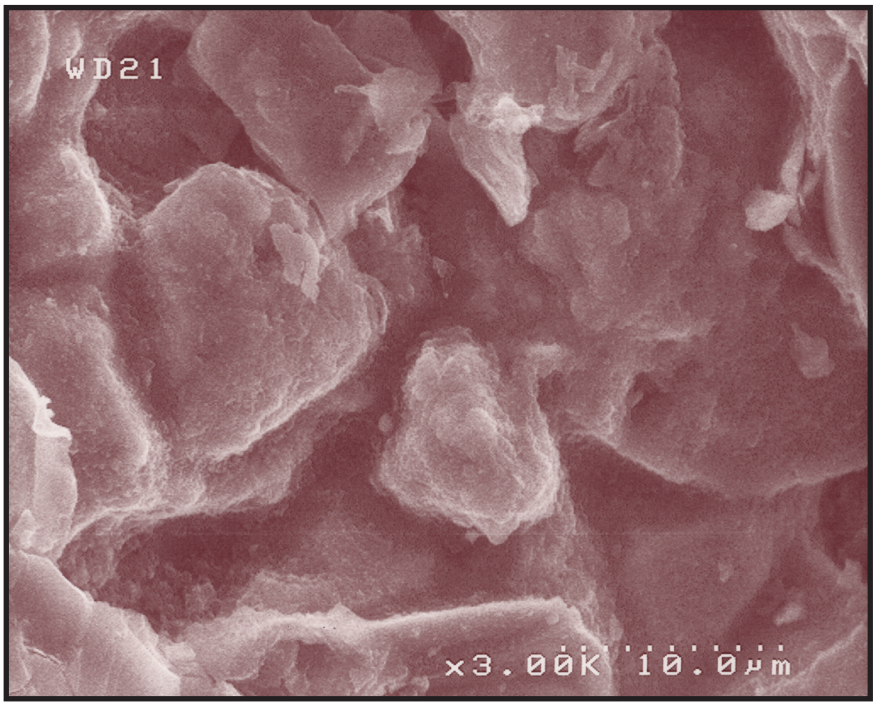


Figure 3.9 - SEM images from porous breccia samples. (a) Euhedral crystal faces present within breccia pores indicates localized quartz growth after brecciation (BB-10); and (b) Coated quartz grains (BB-3). The coating is interpreted to be iron-oxide because of the abundance of iron oxides observed in thin-section.

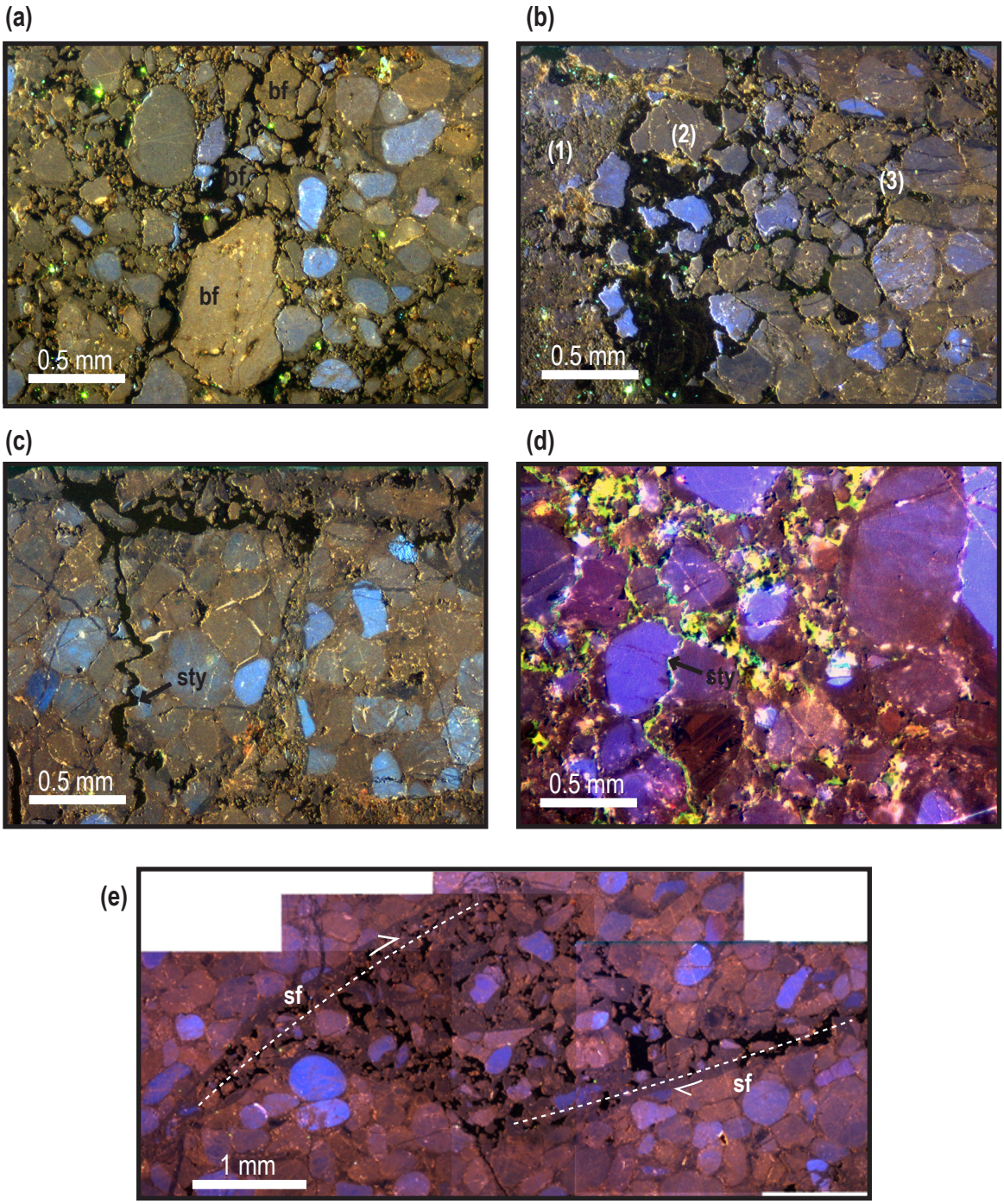


Figure 3.10 - Partially cemented breccias (cont.). All images are CL. Open porosity typically appears dark gray or green, whereas fracture fills and late stage cements appear dark purple or blue. (a) Breccia fragments (bf) with no cement and irregular boundaries (BB-3). (b) Three breccia morphologies: (1) nonporous, fine-grained cataclasite; (2) porous zone of breccia clasts with no cement, irregular boundaries, and abundant porosity; and (3) cemented and partially cemented breccia and grain fragmentation (BB-10). (c) Older stylolite (sty) truncated by younger breccia (BB-10). (d) Partially healed breccia with younger stylolite (sty) (BB-3); (e) Breccia developed at overlap between two small shear fractures (sf), resulting in a dilational jog (BB-10).

development. Samples from zones of intense fractures near faults, BB-2 and BB-6, typically show abundant microscale dilatant shear fractures with grain disaggregation and breccia at fracture intersections. As at the mesoscale, fractures become less abundant with increasing distance from the faults and fractures transition from shear to joints that lack disaggregation.

Microstructural Textures of Background Samples

Background samples adjacent to the damage zone, although not undeformed, lack the intense fractures found within the damage zone samples. Typically, these samples contain few if any transgranular features, and intragranular structures include undulatory extinction, deformation lamellae, fluid inclusion planes, and non-planar fluid inclusions (Fig. 3.11).

Microstructural Abundances

To assess the relative importance of deformation mechanisms during formation of the damage zone, abundance of 14 microstructures was pointcounted. Approximately 250 grains were counted per thin section (Table 3.2). Counts were made on a grid spacing greater than grain size, and all microstructures in a grain were counted, yielding counts greater than the population of approximately 250 grains. The reliability of the abundances are a function of both the total number of grains counted and the number of grains in a given category. Counts of greater than 250 grains are accurate to approximately ± 5% for the 95% confidence level (Van Der Plas and Tobi, 1965; Wu and Groshong, 1991).

The three background samples (Table 3.2, Fig. 3.2a) have comparable microstructural abundances to regional Tuscarora Sandstone samples (Onasch and Dunne, 1993). Undulatory extinction is abundant, intragranular fluid inclusion planes are common, grains lacking microstructures are similar with abundances of approximately 30%, and cataclastic textures are rare. A key difference between the Cave Mountain and regional background samples is a lack of microveins within the Cave Mountain samples when compared with regional values, which elsewhere reach up to 25%.

Both background and damage zone samples share similar abundances of non-planar fluid inclusions, undulatory extinction, and sutured grain boundaries that we interpret to be pre-faulting, if not pretectonic in age. This suite of microstructures is typically interpreted to have formed during early Alleghanian layer-parallel shortening (Couzens et al., 1993; Onasch and Dunne, 1993). In contrast, damage zone samples have greater abundances of intragranular and transgranular healed fractures, which are almost absent within background samples.

As expected, damage zone samples from secondary faults have consistently greater abundances of porous breccia, disaggregated zones, and healed cataclasite textures as compared to other domains.

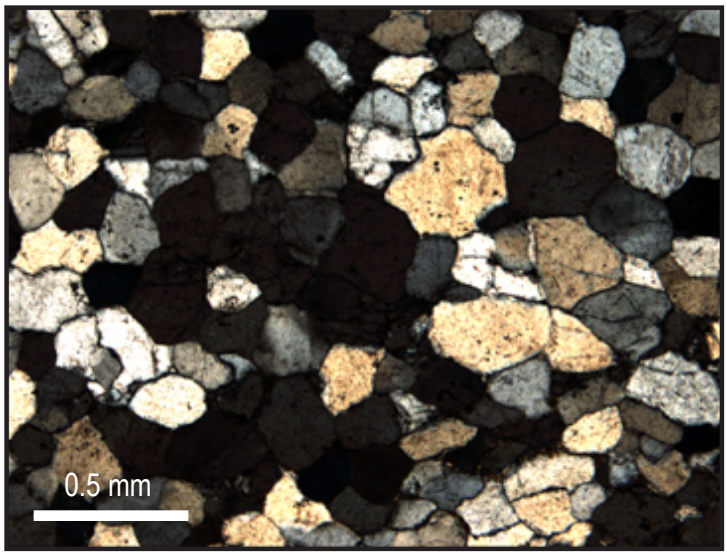


Figure 3.11 - Photomicrograph of a background sample. Sample BB-18 contains coherent grains and lacks many of the brittle or solution-related transgranular structures found in the damage zone.

Table 3.2 - Microstructural abundances classified by primary deformation process.

		BRITTLE																CRYSTAL-PLASTIC						PRESSURE SOLUTION				NO STRUCTURE	
		Intragranular		Transgranular		Fluid Inclusions		Open		Transgranular		Microfault		Zone of Grain		Cataclasite/		Deformation		Patchy		Undulatory		Stylolite		Irregular/Suture			
	Total Grains	%	#	%	#	%	#	%	#	%	#	%	#	%	#	%	#	%	#	%	#	%	#	%	#	%	#	%	#
DAMAGE ZONE SAMPLES																													
Damage Zone - Horses																													
BB-1	254	39.8	101	0	0	65.4	166	0.0	0	2.0	5	0.0	0	0.0	0	0.4	1	13.8	35	0.8	2	43.3	110	2.0	5	5.9	15	5.5	14
BB-2	250	40.0	100	1.2	3	62.0	155	7.6	19	0.4	1	0.0	0	2.0	5	0.0	0	1.2	3	4.0	10	36.4	91	0.4	1	0.0	0	12.8	32
BB-4	250	56.4	141	0.8	2	40.8	102	0.0	0	6.4	16	0.0	0	0.0	0	0.0	0	11.2	28	2.8	7	26.8	67	0.0	0	0.0	0	13.6	34
BB-5	258	44.2	114	0.8	2	46.5	120	0.0	0	0.4	1	0.0	0	0.0	0	0.0	0	10.9	28	2.3	6	27.9	72	0.0	0	0.0	0	15.5	40
BB-6	255	22.4	57	0.0	0	41.6	106	3.9	10	0.8	2	0.0	0	16.1	41	0.0	0	2.0	5	2.7	7	15.7	40	0.0	0	0.0	0	16.5	42
BB-7	250	40.0	100	2.0	5	74.8	187	6.0	15	4.4	11	0.4	1	0.8	2	0.0	0	1.6	4	3.2	8	39.6	99	4.0	10	2.4	6	4.4	11
BB-8	250	34.0	85	12.4	31	41.6	104	0.4	1	0.8	2	0.0	0	0.0	0	0.0	0	6.0	15	4.8	12	34.0	85	0.4	1	4.0	10	10.4	26
BB-9	250	54.4	136	4.4	11	71.2	178	6.4	16	0.8	2	0.0	0	0.0	0	0.0	0	3.6	9	3.2	8	35.2	88	0.0	0	0.4	1	11.2	28
BB-12	250	23.6	59	0.0	0	46.0	115	0.0	0	0.4	1	0.0	0	0.0	0	0.0	0	8.0	20	0.8	2	30.4	76	0.0	0	6.8	17	25.2	63
BB-13	251	53.4	134	0.0	0	57.0	143	0.4	1	6.4	16	0.8	2	3.6	9	3.6	9	6.8	17	7.2	18	38.6	97	0.0	0	0.8	2	7.6	19
BB-14	254	26.0	66	0.0	0	44.5	113	0.0	0	1.6	4	0.0	0	0.0	0	0.0	0	7.1	18	3.1	8	46.5	118	0.0	0	0.0	0	20.9	53
BB-23	250	44.0	110	0.0	0	72.4	181	2.8	7	0.4	1	0.0	0	0.0	0	0.0	0	2.4	6	3.2	8	24.0	60	0.0	0	0.0	0	8.8	22
BB-24	254	48.0	122	5.5	14	70.1	178	0.0	0	2.0	5	0.0	0	0.0	0	0.0	0	18.9	48	4.3	11	51.6	131	0.0	0	0.8	2	5.9	15
	Average	40.5	101.9	2.1	5.2	56.4	142.2	2.1	5.3	2.1	5.2	0.1	0.2	1.7	4.4	0.3	0.8	7.2	18.2	3.3	8.2	34.6	87.2	0.5	1.3	1.6	4.1	12.2	30.7
Damage Zone - Fault																													
BB-3	254	42.1	107	0.8	2	64.6	164	2.4	6	0.8	2	0.0	0	66.9	170	0.8	2	2.0	5	2.4	6	20.9	53	1.2	3	0.4	1	0.0	0
BB-10	250	38.4	96	0.0	0	67.2	168	1.2	3	6.0	15	0.0	0	43.6	109	1.6	4	3.2	8	5.2	13	31.2	78	0.0	0	0.0	0	2.0	5
BB-11	254	41.3	105	14.2	36	11.0	28	0.8	2	12.2	31	0.8	2	0.0	0	24.0	61	4.3	11	7.1	18	59.1	150	2.0	5	4.7	12	1.2	3
BB-17	250	36.0	90	0.4	1	52.8	132	0.4	1	12.0	30	0.0	0	2.4	6	58.0	145	2.0	5	4.4	11	40.0	100	0.0	0	0.0	0	0.0	0
BB-21	250	2.8	7	0.0	0	61.6	154	0.8	2	14.8	37	0.0	0	0.0	0	42.4	106	0.4	1	8.4	21	28.4	71	0.4	1	1.6	4	0.4	1
	Average	32.1	81.0	3.1	7.8	51.4	129.2	1.1	2.8	9.2	23.0	0.2	0.4	22.6	57.0	25.4	63.6	2.4	6.0	5.5	13.8	35.9	90.4	0.7	1.8	1.3	3.4	0.7	1.8
DAMAGE ZONE BACKGOUND SAMPLES																													
BB-18	256	24.2	62	0.0	0	38.3	98	0.0	0	0.8	2	0.0	0	0.0	0	0.0	0	2.3	6	2.7	7	30.5	78	0.0	0	2.7	7	30.1	77
BB-19	252	26.6	67	0.0	0	56.3	142	0.0	0	0.0	0	0.0	0	0.0	0	0.0	0	1.6	4	2.8	7	34.5	87	0.0	0	0.0	0	25.8	65
BB-20	250	14.0	35	0.4	1	50.8	127	0.0	0	0.8	2	0.0	0	0.8	2	0.0	0	2.0	5	2.4	6	26.8	67	0.0	0	0.8	2	23.6	59
	Average	21.6	54.7	0.1	0.3	48.5	122.3	0.0	0.0	0.5	1.3	0.0	0.0	0.3	0.7	0.0	0.0	2.0	5.0	2.6	6.7	30.6	77.3	0.0	0.0	1.2	3.0	26.5	67.0
CHEVRON FOLD SAMPLES																													
CV-2	253	64.0	162	4.7	12	56.9	144	0.4	1	17.4	44	2.8	7	0.4	1	7.5	19	34.0	86	5.5	14	54.2	137	0.0	0	0.4	1	2.8	7
CV-6	252	76.6	193	22.6	57	72.6	183	3.2	8	40.1	101	0.8	2	0.0	0	4.0	10	14.3	36	10.3	26	41.7	105	6.7	17	1.6	4	0.0	0
	Average	70.3	177.5	13.7	34.5	64.8	163.5	1.8	4.5	28.7	72.5	1.8	4.5	0.2	0.5	5.7	14.5	24.1	61.0	7.9	20.0	47.9	121.0	3.4	8.5	1.0	2.5	1.4	3.5

Fault zones also have a greater abundance of patchy extinction, but do not have elevated abundance of either undulatory extinction or deformation lamellae, which may indicate that “patchy” extinction within fault samples results from grain fracturing and healing, rather than dislocation-related processes (Onasch and Dunne, 1993).

4. FLUIDS WITHIN THE DAMAGE ZONE

Fluids can influence the formation of damage zones. For example, pore fluid pressure reduces normal stresses and can trigger dilatant fracturing (Secor, 1965). Transient fluid pressure differentials along dilational jogs or releasing bends also induce fracturing of the wall rock (Sibson, 1987; Tarasewicz et al., 2005). Intragranular water can cause hydrolytic weakening (Kronenberg, 1990), which can enhance both dislocation-related and brittle deformation rates. Diffusion mass transfer processes including microcrack healing are favored by the presence of fluids (Brantley et al., 1990). Because no similar damage zones have been previously described for the Tuscarora Sandstone, we investigate the role of fluid in damage zone development.

4.1 Evidence for Fluids within the Damage Zone

The presence of abundant fluid-inclusion-related structures, euhedral cement overgrowths, some microveins, and a limited number of transgranular stylolites support a chemical role for fluids during damage zone development. Cemented fractures and breccias overprinted by porous breccia and joints are consistent with precipitation from silica-saturated fluids, particularly during early damage zone development. During most later deformation, very little cementation occurred indicating a change in fluid-rock interactions. CL and SEM imagery show abundant euhedral crystal faces and partially cemented microveins as well as solution features and textures such as stylolites and corroded surfaces. Questions that arise from this evidence are: Did changes in fluid composition trigger chemical changes from precipitation to solution, and is this change a critical element in the creation of porous fault rocks? To answer these questions, we describe the results from fluid inclusion microthermometry and Fourier Transform Infrared Spectroscopy (FTIR).

4.2 Fluid Inclusion Microthermometry

Doubly polished thick sections (50–100 μm), prepared using the methods of Reynolds and Goldstein (1999), were used for fluid inclusion microthermometry to gain insight into fluid composition. Fluid inclusions, in planar arrays or as isolated inclusions, larger than 5 μm were analyzed in seven samples: porous fault breccias (BB-3 and BB-17), intensely fractured horse samples (BB-2 and BB-3), background sample (BB-19), and outside the damage zone in the outcrop-scale chevron fold (CV-2 and CV-6) (Fig. 3.1). For each sampled inclusion, the homogenization temperature (T_h) and solid melting (sublimation) temperature (T_m) were recorded, depending on inclusion type (Figs. 4.1, 4.2).

Based on the heating and freezing behavior, two types of inclusions were identified: abundant single-phase methane-rich and rare two-phase aqueous inclusions. The methane-rich inclusions are

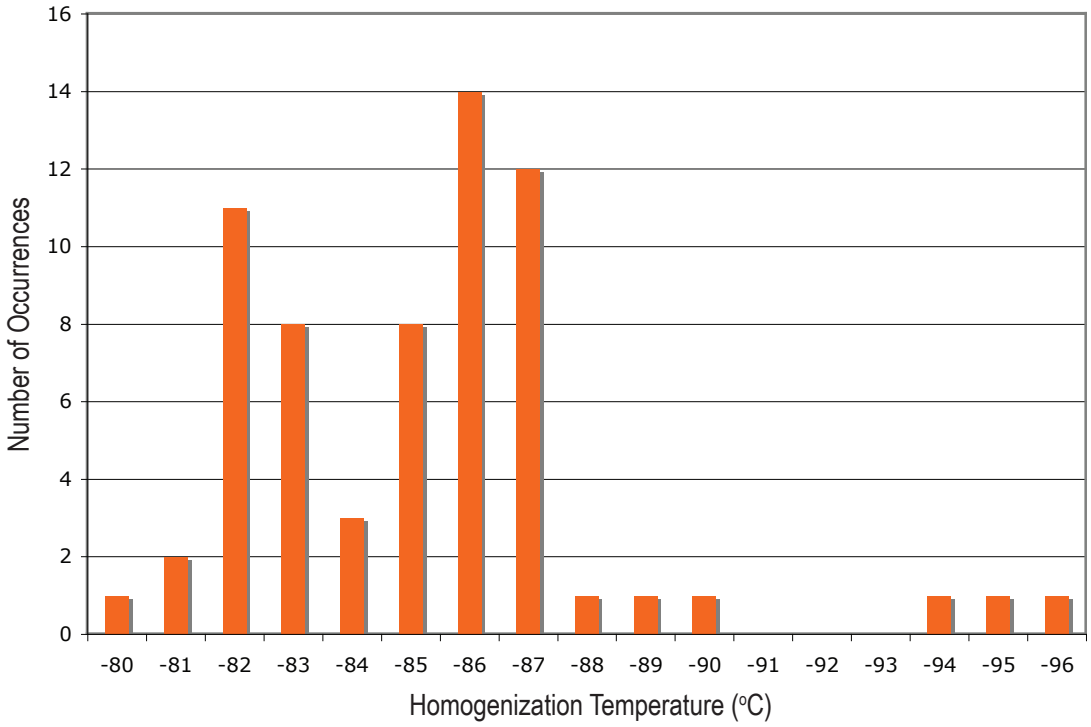


Figure 4.1 - Histogram of homogenization temperatures (T_h) for CH_4 inclusions. Data courtesy of C.Onasch.

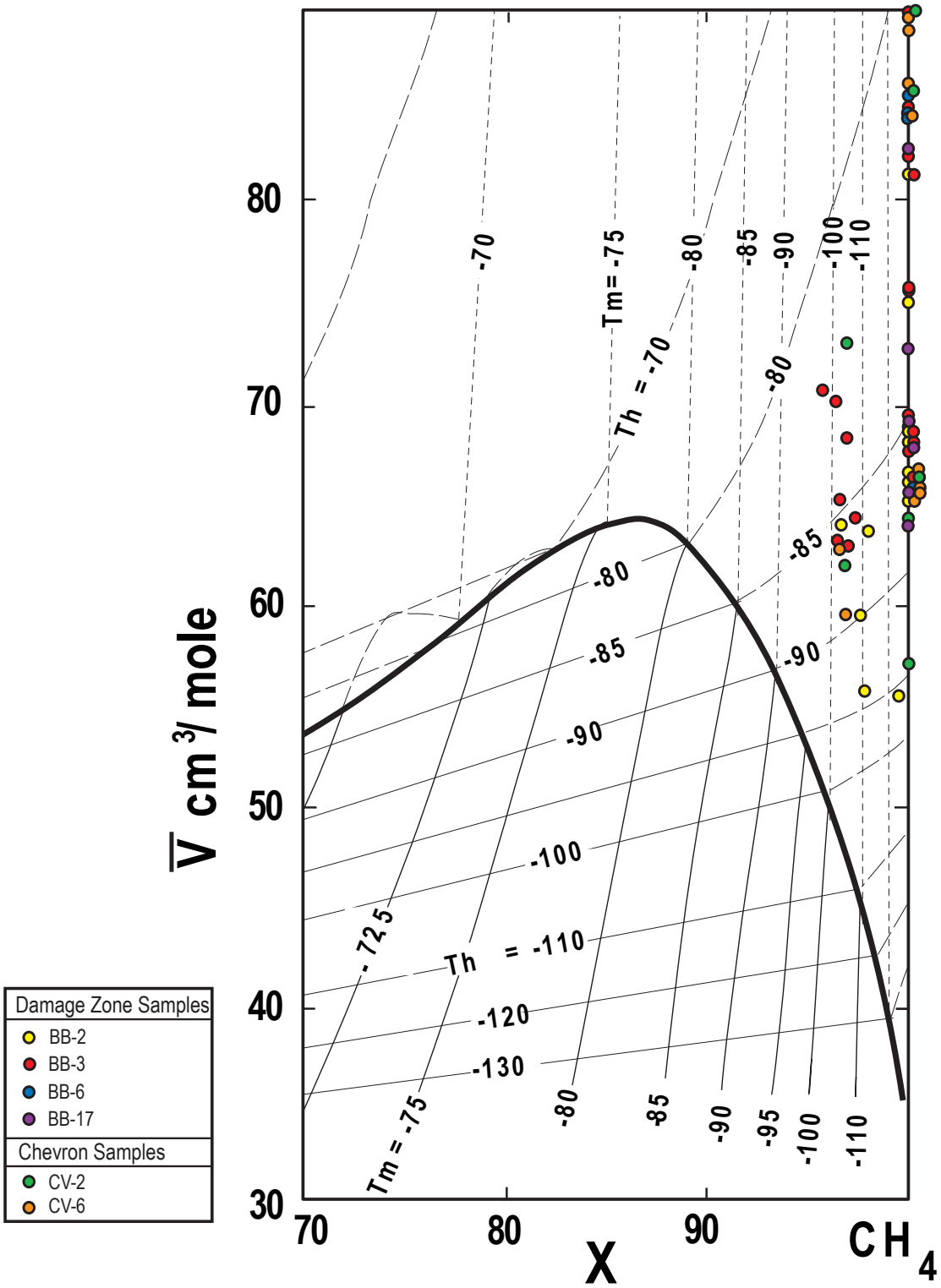


Figure 4.2 - VX (Molar Volume/Composition) diagram for CH_4-CO_2 fluid inclusions. Inclusions are plotted based on the CO_2 solid melting (sublimation) (T_m) and the hydrocarbon homogenization temperature (T_h), giving the composition of each inclusion. Inclusions that plot on the y-axis are >98% CH_4. All temperatures are in degrees Celsius (data courtesy of C.Onasch) (after van den Kerkhof, 1988).

colorless, monophase at room temperature, and are <2 to >10 μm in their long dimension. When cooled to -150° C, they contain three phases: a liquid, a vapor, and a solid. The solid is CO_2 (triple point temperature of -56.5° C) and the liquid and vapor are methane (CH_4) (critical temperature of -82.4° C). Upon heating, the solid melts (sublimates) followed by homogenization of the vapor bubble to a liquid. Plotting the solid melting (sublimation) (T_m) and homogenization (T_h) temperatures (Fig. 4.1) on a VX diagram of the CO_2-CH_4 system (van den Kerkhof, 1988, 1990) (Fig. 4.2) allows estimation of the fluid composition. Most of the inclusions are greater than 96% CH_4 with many likely to be pure methane. The aqueous inclusions are colorless and show two phases at room temperature, liquid and vapor that homogenize at temperatures above 168° C. Freezing behavior was not determined due to their small size (<4 μm) so the salinity could not be determined.

Most fluid inclusions in the damage zone and chevron fold samples are methane-rich. They occur along fluid inclusion planes, on grain boundaries, and as isolated inclusions within grains. Although methane-rich inclusions are common in Ordovician through Devonian strata within the central Appalachians (Evans and Battles, 1999), they are rare or absent in the Tuscarora Sandstone outside the study area (Onasch, 1990; Harrison and Onasch, 1999; O'Kane, 2005; C. Onasch, pers. comm.). Thus, the occurrence of methane-rich inclusions in the Tuscarora Sandstone in the culmination of the Cave Mountain anticline may have significance.

Aqueous inclusions within the damage zone are rare and yield highly variable homogenization temperatures suggesting that they are inherited from plutonic or metamorphic source terranes. Background sample BB-19, however, contained aqueous inclusions along fluid inclusion planes that yielded consistent homogenization temperatures indicating that they formed in-situ. Even in this sample, the methane-rich inclusions outnumbered the aqueous inclusions by at least 2:1.

4.3 Microscale Water Distribution from Fourier Transform Infrared Spectroscopy

Intracrystalline water concentration was measured for nine damage zone samples using Fourier Transform Infrared Spectroscopy (FTIR) to investigate variations in water content and distribution within the damage zone (Kronenberg and Wolf, 1990). The water concentration was determined using the 3400 nm peak on the infrared (IR) spectra using a Perkin Elmer Spectrum GX Fourier Transform Infrared Spectrometer with microscope accessory.

Samples for FTIR analysis were chosen to represent the variety of deformational textures within the damage zone: a relatively undeformed background sample, four horse samples from zones of varying fracture intensities, three porous breccias, and one healed breccia/cataclasite. 15 FTIR analyses, chosen to reflect a variety of grain types and microstructural features, were completed on each sample. An effort was

made to sample relatively undeformed grains, grains containing abundant brittle intragranular structures, and grains within and adjacent to transgranular structures such as microfractures, cataclasite, and stylolites. To assess general trends across the damage zone and minimize the affects of inheritance, water concentrations for the 15 measurements were averaged for each sample.

Water concentration (H x 10^6 Si) for each sample location was determined using the following equation:

$$\textbf{\textit{Water Concentration}} = \left(1.05 \times Acor\right) / t \times 10^4$$

where, A_{cor} is the area under the absorption curve determined through peak integration of the raw sample and background spectra, and t is the thickness of the sample analyzed (Nakashima et al., 1995).

The lowest average water concentrations (Table 4.1, Fig. 4.3), between 3,519 and 5,665 H x 10^6 Si occurred in relatively undeformed background samples and from porous breccias or samples from intensely fractured zones. These breccia and intensely fractured samples contain abundant brittle deformation, and lack pervasive, quartz cements and fracture fills. Internal block damage zone samples yielded water concentrations between 6,429 and 8,218 H x 10^6 Si, and the greatest average water concentrations, between 10,480 and 15,090 H x 10^6 Si, occurred in fault samples, a healed cataclasite and relatively porous breccia. Previous studies using FTIR on naturally deformed, quartz-rich rocks have reported water concentrations between 1,400 and 8,000 H x 10^6 Si (e.g., Kronenberg and Wolf, 1990), indicating that several samples from the damage zone have very high intragranular water concentrations.

Elevated water concentrations within samples from the damage zone may indicate either increased abundance of intragranular fractures, and thus ability to trap intragranular fluid; or dislocation-related deformation where dislocation cores provide a diffusion pathway for water molecules (Kronenberg and Wolf, 1990). Because dislocation-related deformation is not abundant in most damage zone samples, it is likely that elevated water concentrations result from increased abundance of trapped fluid in microfractures. The two samples with the greatest water concentrations are from rocks immediately adjacent to fault 2, at the southeastern edge of the damage zone exposure. Fault and internal samples with significantly lower water concentrations, between 3,519 and 6,429 H x 10^6 Si, are from zones adjacent to faults 3 and 4, at the northwestern end of the damage zone exposure. Differences in water concentrations between samples near individual faults may indicate different kinematic or fluid histories along these surfaces during damage zone development. Despite local variations in water concentration, elevated water content in samples from the damage zone as compared to water content in the background samples suggest that water, in addition to methane, was present during damage zone development.

Table 4.1 - Fourier transform infrared spectroscopy (FTIR) data. Water concentrations are in $Hx10^6$ Si.

Sample Number	Maximum	Minimum	Average	Sample Classification	Location
BB-2	9238.9	836.2	*3519.1*	horse	Near Fault 4
BB-19	*7616.6*	551.6	*3581.8*	background	-
BB-3	11949.5	2477.0	*5588.6*	breccia	Fault 3
BB-10	12722.8	1767.8	5665.9	breccia	Fault 3
BB-6	14972.7	2417.2	6429.0	horse	Near Fault 4
BB-8	11758.7	2904.3	*6652.4*	horse	Horse C
BB-24	17653.7	4043.4	*8218.5*	horse	Horse B
BB-11	14974.0	887.7	10480.6	healed breccia/cataclasite	Fault 2
BB-17	21363.7	6945.9	15090.0	healed breccia	Fault 2

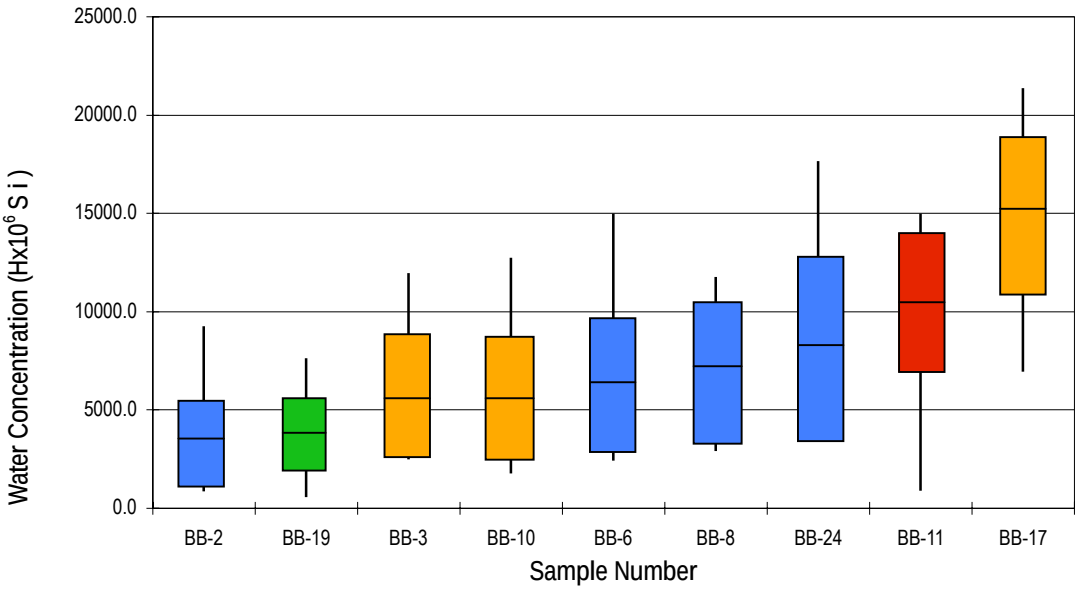


Figure 4.3 - Water concentration from FTIR. Colored box is one standard deviation: blue - horse, green - background, orange - breccia, red - cataclasite. Black vertical line represents minimum and maximum values. Black horizontal line is average.

5. DISCUSSION

5.1 Fluids in the Damage Zone

Variation in temperature, pressure, pH, salinity, and composition of aqueous fluids affect quartz precipitation and dissolution (Brantley et. al, 1990; Azaroual et al., 1997). Methane, however, is chemically inert to quartz, and does not precipitate nor dissolve quartz. Methane and aqueous fluids in combination are more problematic. In many cases, methane, even where water-bearing fluids are present, can inhibit quartz precipitation by blocking quartz diffusion pathways and preventing nucleation and crystal growth (Houseknecht and Spötl, 1993; Worden et al. 1998; Marchand et al., 2000; 2002; Haszeldine et al., 2003).

Healed structures including breccias, cataclasite, microveins, and fluid inclusion planes; FTIR analysis; aqueous inclusions within the background sample; and previous fluid-inclusion work (Onasch, 1993; Evans and Battles, 1999; O'Kane, 2005) indicate that aqueous fluid capable of quartz precipitation was important in the Tuscarora Sandstone during Alleghanian foreland deformation. However, the fluid present within fluid inclusion planes in the damage zone is dominantly methane, which is atypical of fluid chemistry for the inclusions trapped in Alleghanian fractures in the Tuscarora Sandstone.

Source of Methane in the Damage Zone

Previous fluid inclusion investigations of the lower and middle Paleozoic strata in the Appalachians and the Tuscarora Sandstone, in particular, have documented two-phase aqueous inclusions, high-salinity brines, and methane inclusions (Onasch, 1990; Evans and Battles, 1999; Harrison and Onasch, 1999; O'Kane, 2005; C. Onasch pers. comm.). Evans and Battles (1999) recognized three hydrostratigraphic systems within the Paleozoic section of the Appalachian Valley and Ridge. The system from the Ordovician Trenton Formation through the Devonian Helderberg Formation, which includes the Tuscarora Sandstone, acted as a regional aquitard containing in-situ high-salinity, methane-saturated brines. Although no samples from the Tuscarora Sandstone were analyzed, methane inclusions dominated the Martinsburg Formation and were present in stratigraphic units through the lower Devonian (Evans and Battles, 1999). Other studies, which have included samples from the Tuscarora Sandstone, have found two-phase aqueous inclusions with few or no methane-rich inclusions (O'Kane, 2005, C.Onasch, pers.comm.). Therefore, although methane inclusions are abundant within the underlying Martinsburg Formation and some overlying units, they are atypical in the Tuscarora Sandstone.

Four hydrocarbon source rocks have been identified within the Appalachian Basin, including the Cambrian Rome Formation, Ordovician shales including the Martinsburg Formation, Devonian Shales including the Needmore and Marcellus Formations, and Pennsylvanian coal sequences (Roen and Walker, 1996). Methane-rich fluids in the Tuscarora Sandstone likely originated within either the Martinsburg

Formation or Devonian Shales. Because of its proximity, the Ordovician Martinsburg Formation seems the most likely source for the methane found within the Tuscarora Sandstone in the Cave Mountain anticline. The forethrust and backthrust system within the Cave Mountain anticline would have acted as a fluid conduit system for methane-rich fluid from the underlying Martinsburg Formation. This model requires that the backthrust system root to the underlying thrust fault, and that this underlying fault offsets the Martinsburg Formation (Figs. 2.2, 3.1). The forethrust offsets over 1000 m of Silurian stratigraphy at the ground surface, and it likely persists through 200 m of the underlying Juniata Formation to offset the Martinsburg Formation.

Methane would have risen along the forethrust and accessed both the chevron-fold hinge through minor faults and the damage zone along a backthrust. This methane-rich fluid may have mixed with and locally displaced the resident aqueous fluid. The location of the damage zone along the fault network/fluid conduit system would have allowed for direct influx of fluids into the damage zone from the fault that may have resulted not only in abundant methane within the zone, but also locally elevated fluid pressures. The damage zone would have been exposed not only to in-situ fluids, but also transient fluids moving along the fault conduit system. Fluid chemistry and pressure within the damage zone are therefore very likely to have changed over time.

5.2 Damage Zone Development

Evidence for Elevated Fluid Pressures During Damage Zone Development

Within fault-bounded horse C, near fault-normal joints are locally pervasive (Figs. 3.2a, 5.1). Such joints form in zones bounded by two sub-parallel and downstepping en-echelon faults at an extensional step-over, where the magnitude of the local minimum principal stress decreases and extension fractures are favored (Ohlmacher and Aydin, 1997). The local principal stress orientations change within the extensional step-over as a result of a decrease in the frictional resistance to near zero along the fault, so that the angle between joints and the master fault will increase as the coefficient of friction decreases to nearly frictionless (Ohlmacher and Aydin, 1997).

Coulomb frictional resistance along a fault is defined as:

$$T_f = (\sigma_n - \rho_f)\,\mu + c,$$

where T_f is the frictional resistance, σ_n is the normal stress to the fault, ρ_f is the fluid pressure, μ is the coefficient of internal friction, and c is the cohesion. Low frictional resistance along a fault can be accomplished by a decrease in effective normal stress, $\sigma_n - \rho_f$, resulting from decreased normal stresses, or

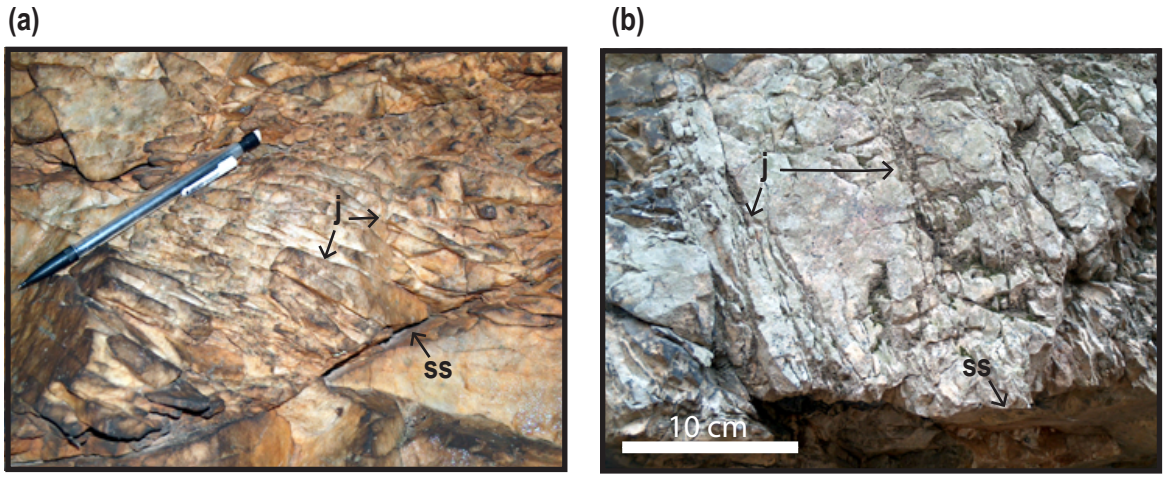


Figure 5.1 - Joints forming sub-normal to fault surfaces. (a) Small, higher order slip surface (ss) with intense near fault normal jointing (j). (b) Second-order slip surface(ss) with near fault normal joints.

increased fluid pressure. During orogenesis driven by a subhorizontal maximum compression, fluid pressures must approach the magnitude of the lithostatic load for frictional resistance along thrusts to be low (Hubbert and Rubey, 1959; Srivastava and Engelder, 1990; Ohlmacher and Aydin, 1997). Given burial at depth of greater than 5 km in a continually evolving foreland thrust belt, the occurrence of this type of joint pattern is best explained by a relatively fast state change, such as a fluctuation in fluid pressure along the bounding fault zones. Also, given the lack of silica cement in the fault zones and joints, the possibility exists the fluid pressure increase was achieved with a methane-dominated fluid. Because methane is more compressible than aqueous fluids, methane may enhance fracture propagation and thus increase the ability of the host rock to fracture (Lacazette and Engelder, 1992).

Formation of an Extensional Relay in a Thrust System

The damage zone is interpreted to have developed as a relay between en-echelon backthrusts. An alternative explanation is that the damage zone is developed as a dilational jog along a single fault. The relay interpretation is favored for the following two reasons: First, the Tuscarora Sandstone in the vicinity of the damage zone lacks a stratigraphic or structural heterogeneity that would have caused a perturbation of the stress field, leading to thrust propagation with a jog. Second, the number, position, and displacement of backthrusts in the Cave Mountain anticline vary along strike (Fig. 2.2). These variations support an interpretation where two faults propagated laterally and overlapped to create a potential relay zone. The following discussion assumes the damage zone developed from an initial fault relay, rather than a fault jog (Fig. 5.2).

Extensional relay zones are typically linked or breached by faults formed at 45º to 90º to the overlapping faults (Peacock and Sanderson, 1994; Walsh et al., 1999; Ferrill and Morris, 2001; Kim et al., 2004). This type of breaching was likely the first step in damage zone development, although bedding to fault geometries, fault-rock characteristics, and fracture distributions indicate that breaching behavior differed for the two initial faults, 1 and 4 (Figs. 5.2a, b, c).

Breach initiation of fault 1 and adjacent fault 2 involved bedding rollover along the fault, early cataclasite (BB-11), and development of complex secondary fault systems in the rollovers. In contrast, breach initiation of fault 4, including fault 3, generated acute bedding cutoff geometries and a combination of cataclasite and breccias. These structural differences indicate that breach initiation for fault 1 involved a combination of greater frictional resistance or displacement gradient behavior when compared with fault 4 (Twiss and Moores, 1992; Wickham, 1995, Grassmann et al., 2005). Continued propagation led to complete breaching and displacement transfer between faults 1 and 4 (Fig. 5.2c).

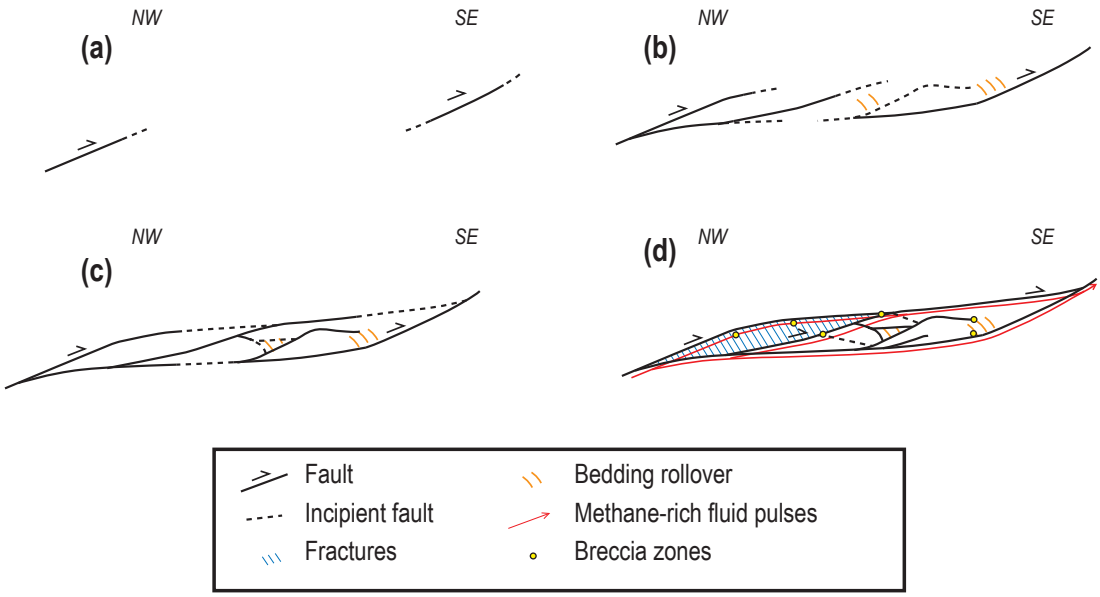


Figure 5.2 - Damage zone development. (a) Initial overlap of independent faults; (b) and (c) Initial propagation of relay structures; (d) Breaching of relay structures creating fault bounded horses. Pulses of methane-rich fluid coinciding with modest fault displacements results in the formation of joints and breccias.

The damage zone contains well-preserved porous breccias and near fault-normal joints in horse C that show no evidence for reactivation as shear or solution structures. Such features are interpreted to have formed very late during damage zone development and were associated with only modest displacements and elevated fluid pressures, likely achieved with a methane-rich fluid that prevented cementation (Fig. 5.2d). Porous breccias preferentially developed at fault branches, fault bends, and fault tips. Breccia that developed at fault branches and bends likely formed through a hierarchical fragmentation process, involving the reactivation of pre-existing extension fractures and the formation of new, higher-order splay fractures with continued slip along the fault. Fragmented clasts were rotated along the faults, causing further comminution and attrition of grains. In contrast, breccia located at fault tips likely developed from tipping-effects.

6. CONCLUSIONS

1. A damage zone developed in the well-cemented Tuscarora Sandstone is comprised of a network of NW-dipping backthrusts that are linked by multiple higher-order faults and bound a zone of intense extensional fractures and dilational breccias. These structures transfer displacement upsection from the northwest to southeast and acted as a relay zone within a backthrust system.

2. Although the sandstone contains evidence for aqueous fluids, abundant methane inclusions are present in the damage zone and are atypical for Alleghanian structures in the Tuscarora Sandstone. The backthrust network likely acted as a fluid conduit system, bringing methane-rich fluids up from the underlying Ordovician Martinsburg Formation. Methane was important to damage zone development in two ways: (1) methane likely enhanced the effects of pore fluid pressure, facilitating brittle fracturing; and (2) methane inhibited the nucleation and precipitation of quartz, preventing the complete healing of open fractures and breccia pores, particularly during late damage zone development.

3. Pervasive, fault-normal joints in a fault-bounded horse in the northwestern damage zone indicate formation between two near-frictionless faults. The decrease in frictional resistance is likely a result of increased pore fluid pressure.

4. The damage zone developed at an extensional step-over between two independent, laterally propagating backthrusts. Continued displacement resulted in breaching of the relay with differences in breaching behavior between backthrusts that were likely the result of greater frictional resistance or displacement gradient behavior along the southeastern faults. Late displacement with a pulse of methane-rich fluid formed mesoscale joints and porous breccia.

5. The damage zone structures comprise a zone of localized high porosity and permeability within a well-cemented quartz arenite. Similar zones should be expected to develop in extensional linkages between faults where cementation is inhibited, and where fluid pressures enhance dilatancy.

REFERENCES CITED

Antonellini, M.A., Aydin, A., Pollard, D.D., 1994. Microstructure of deformation bands in porous sandstones at Arches National Park, Utah. Journal of Structural Geology 16, 941-959.

Aydin, A., 1978. Small faults formed as deformation bands in sandstone. Pure and Applied Geophysics 116, 913–930.

Azaroual, M., Fouillac, C., Matray, J.M.,1997. Solubility of silica polymorphs in electrolyte solutions, I. Activity coefficient of aqueous silica from 25° to 250°C, Pitzer's parameterisation. Chemical Geology 140, 155-165.

Blenkinsop, T.G., Rutter, E.H., 1986. Cataclastic deformation of quartzite in the Moine thrust zone. Journal of Structural Geology 8, 669-681.

Brantley, S.L., Evans, B., Hickman, S.H., Crerar, D.A., 1990. Healing of microcracks in quartz; implications for fluid flow. Geology 18, 136-139.

Caine, J.S., Evans, J.P., Forster, C.B, 1996. Fault zone architecture and permeability structure. Geology 24, 1025-1028.

Chester, F.M.,Logan, J.M., 1986. Implications for mechanical properties of brittle faults from observations of the Punchbowl fault zone, California. Pure and Applied Geophysics 124, 79-106.

Cotter, E. ,1983. Shelf, paralic, and fluvial environments and eustatic sea-level fluctuations in the origin of the Tuscarora Formation (Lower Silurian) of central Pennsylvania. Journal of Sedimentary Petrology 53, 25-49.

Couzens, B.A., Dunne, W.M., 1994. Displacement transfer at thrust terminations; the Saltville Thrust and Sinking Creek Anticline, Virginia, U.S.A. Journal of Structural Geology 16, 781-793.

Couzens, B.A., Dunne, W.M., Onasch, C.M., Glass, T.,1993. Strain variations and three-dimensional strain factorization at the transition from the Southern to the Central Appalachians. Journal of Structural Geology 15, 451-464.

Crider, J.G., Peacock D.C.P., 2004. Initiation of brittle faults in the upper crust: a review of field observations. Journal of Structural Geology 26, 691-707.

Davatzes, N.C., Aydin, A., 2003. Overprinting faulting mechanisms in high porosity sandstones of SE Utah. Journal of Structural Geology 25, 1795-1813.

Davatzes, N.C., Eichhubl, P., and Aydin, A., 2005. Structural evolution of fault zones in sandstone by multiple deformation mechanisms; Moab Fault, southeast Utah. Geological Society of America Bulletin 117, 135-148.

Diecchio, R.J., Dennison, J.M. 1996. Silurian stratigraphy of central and northern Virginia and adjacent West Virginia. In: Broadhead, T.W. (Ed.), Sedimentary environments of Silurian Taconia; fieldtrips to the Appalachian and southern craton of eastern North America, University of Tennessee, Knoxville, 107-127.

Dorsch, J., Driese, S.G., 1995. The Taconic foredeep as sediment sink and sediment exporter: implications for the origin of the white quartzarenite blanket (upper Ordovician – lower Silurian) of the central and southern Appalachians. American Journal of Science 295, 201-243.

Dransfield, B.J., Groshong, R.H., Jr., 1988. Deformation mechanisms and hinge geometries in folded multilayers composed of a single stiff lithology. Geological Society of America Abstracts with Programs 20, 57.

Dunne, W.M., 1996. The role of macroscale thrusts in the deformation of the Alleghanian roof sequence in the central Appalachians: a re-evaluation. American Journal of Science 296, 549-575.

Evans, M.A., Battles, D.A., 1999. Fluid inclusion and stable isotope analyses of veins from the central Appalachian Valley and Ridge Province; implications for regional synorogenic hydrologic structure and fluid migration. Geological Society of America Bulletin 111, 1841-1860.

Ferrill, D.A., Morris, A.P., 2001. Displacement gradient and deformation in normal fault systems. Journal of Structural Geology 23, 619-638.

Flodin, E.A., Aydin, A., 2004. Evolution of a strike-slip fault network, Valley of Fire State Park, southern Nevada. Geological Society of America Bulletin 116, 42-59.

Gallagher, J.J.,Jr., Friedman, M., Handin, J., Sowers,G.M., 1974. Experimental studies relating to microfracture in sandstone. Tectonophysics 21, 203-247.

Gerritsen, S.S., 1988. Structural analysis of the Silurian-Devonian cover in the Smoke Holes, WV. M.S. Thesis, West Virginia University.

Grassmann, B., Martel, S., Passchier, C., 2005. Reverse and normal drag along a fault. Journal of Structural Geology 27, 999-1010.

Harris, A.G., Harris, L.D., Epstein, J.B., 1977. Conodont color alteration; an index to organic metamorphism. U. S. Geological Survey Professional Paper.

Harrison, M.J., Onasch, C.M., 2000. Quantitative assessment of low-temperature deformation mechanisms in a folded quartz arenite, Valley and Ridge Province, West Virginia. Tectonophysics 317, 73-91.

Haszeldine, R.S., Cavanagh, A.J., England, G.L., 2003. Effects of oil charge on illite dates and stopping quartz cement: calibration of basin models. Journal of Geochemical Exploration 78-79, 373-376.

Hatcher, R.D., Jr., Thomas, W.A., Geiser, P.A., Snoke, A.W., Mosher, S., Wiltschko, D.V., 1989. Alleghanian orogen. In: Hatcher, R.D., Jr., Thomas, W.A., Viele, G.W. (Eds.), The Appalachian-Ouachita Orogen in the United States. The Geology of North America F-2, 233-318.

Houseknecht, D.W., 1988. Intergranular pressure solution in four quartzose sandstones. Journal of Sedimentary Petrology 58, 228-246.

Houseknecht, D. W., Spötl, C., 1993. Empirical observations regarding methane deadlines in deep basins and thrust belts. U.S. Geological Survey Professional Paper 1570, 217–231.

Hubbert, M.K., Rubey, W.W., 1959. Mechanics of fluid-filled porous solids and its application to overthrust faulting, [Part] 1 of Role of fluid pressure in mechanics of overthrust faulting. Geological Society of America Bulletin 70, 115-166.

Ismat, Z., Mitra, G., 2001. Folding by cataclastic flow at shallow crustal levels in the Canyon Range, Sevier orogenic belt, west-central Utah. Journal of Structural Geology 23, 355-378.

Jamison, W.R., Stearns, D.W., 1982. Tectonic deformation of Wingate Sandstone, Colorado National Monument. American Association of Petroleum Geologists Bulletin 66, 2584–2608.

Kim, Y.S., Peacock, D.C.P., Sanderson, D.J., 2004. Fault damage zones. Journal of Structural Geology 26, 503-517.

Kronenberg, A.K., Wolf, G.H., 1990. Fourier transform infrared spectroscopy determinations of intragranular water content in quartz-bearing rocks; implications for hydrolytic weakening in the laboratory and within the Earth. Tectonophysics 172, 255-271.

Lacazette, A., Engelder, T., 1992. Fluid-driven cyclic propagation of a joint in the Ithaca Siltstone, Appalachian Basin, New York. In: Evans, B., Wong, T.F. (Eds.), Fault Mechanics and Transport Properties of Rocks; a Festschrift in Honor of W. F. Brace. Academic Press, San Diego, 297-323.

Laubach, S.E. 2003. Practical approaches to identifying sealed and open fractures. American Association of Petroleum Geologists Bulletin, 87, 561-579.

Lloyd, G.E., Knipe, R.J. 1992. Deformation mechanisms accommodating faulting of quartzite under upper crustal conditions. Journal of Structural of Geology 14, 127-143.

Marchand, A., Haszeldine, S., MacCaulay, C., Swennen, R., Fallick, A., 2000. Quartz cementation inhibited by crestal oil charge: Miller deep water sandstone, UK North Sea. Clay Minerals 35, 201-210.

Marchand, A.M., Smalley, C.P., Haszeldine, R.S., Fallick, A.E., 2002. Note on the importance of hydrocarbon fill for reservoir quality prediction in sandstones. American Association of Petroleum Geologists Bulletin 86, 1561-1571.

Myers, R., Aydin, A., 2004. The evolution of faults formed by shearing across joint zones in sandstone. Journal of Structural Geology 26, 947-966.

Nakashima, S., Matayoshi, H., Yuko, T., Michibayashie, K., Masuda, T., Kuroki, N., Yarnagishi, H., Ito, Y, Nakamura, A., 1995. Infrared microspectroscopy analysis of water distribution in deformed and metamorphosed rocks. Tectonophysics 245, 263-276.

Narahara, D.K., Wiltschko, D.V., 1986. Deformation in the hinge region of a chevron fold, Valley and Ridge Province, central Pennsylvania. Journal of Structural Geology 8, 152-168.

O'Kane, A., 2005. The role of water in grain-scale deformation within the cove fault zone, south-central Pennsylvania. M.S. thesis, Bowling Green State University.

Ohlmacher, G.C. Aydin, A., 1997. Mechanics of vein, fault and solution surface formation in the Appalachian Valley and Ridge, northeastern Tennessee, U.S.A.: implications for fault friction, state of stress and fluid pressure. Journal of Structural Geology 19, 927–944.

Onasch, C.M., 1990. Microstructures and their role in deformation of a quartz arenite from the central Appalachian foreland. Journal of Structural Geology 12, 883-894.

Onasch, C.M., 1993. Assessing brittle volume-gain and pressure solution volume-loss processes in quartz arenite. Journal of Structural Geology 16, 519 – 530.

Onasch, C. M. ,Dunne, W.M., 1993. Variation in quartz arenite deformation mechanisms between a roof sequence and duplexes. Journal of Structural Geology 15, 465–475.

Osborne, M.R., Harrison, M., Onasch, C., Dunne, W., 2003. The influence of primary sedimentary features on fold-hinge development in quartz arenite deformed at low temperature. Geological Society of America Abstracts with Programs 35, 178.

Peacock, D.C.P., Sanderson, D.J., 1994. Geometry and development of relay ramps in normal fault systems. AAPG Bulletin 78, 147-165.

Perry, W.J. Jr., 1978. The Wills Mountain anticline: a study in complex folding and faulting in eastern West Virginia. West Virginia Geological and Economic Survey Publication RI-32.

Reger, D.B., Tucker, R.C., 1924. Mineral and Grant Counties. West Virginia Geologic and Economic Survey County Report.

Reynolds, T.J.,Goldstein, R.H., 1994. Systematics of fluid inclusions in diagenetic minerals. Society of Economic Paleontologists and Mineralogists Short Course 31.

Rohrbaugh, M.B., Jr., Dunne, W.M., Mauldon, M., 2002. Estimating fracture trace intensity, density, and mean length using circular scan lines and windows. American Association of Petroleum Geologists Bulletin 86, 2087-2102.

Roen, J.B., Walker, B.J. (Eds), 1996. The atlas of major Appalachian gas plays. West Virginia Geological and Economic Survey Publication V-25.

Secor, D.T., Jr., 1965. Role of fluid pressure in jointing. American Journal of Science 263, 633-646.

Shipton, Z.K., Cowie, P.A., 2001. Damage zone and slip-surface evolution over μm to km scales in high-porosity Navajo sandstone, Utah. Journal of Structural Geology 23, 1823–1844.

Shipton, Z.K., Cowie, P.A., 2003. A conceptual model for the origin of fault damage zone structures in high-porosity sandstone. Journal of Structural Geology 25, 333-344.

Sibley, D.F., Blatt, H., 1976. Intergranular pressure solution and cementation of the Tuscarora orthoquartzite. Journal of Sedimentary Petrology 46, 881-896.

Sibson, R.H., 1987. Earthquake rupturing as a mineralizing agent in hydrothermal systems. Geology 15, 701-704.

Sites, R.S., 1971. Geology of the Smoke Hole Region in Grant and Pendleton Counties, West Virginia. M.S. Thesis, West Virginia University.

Sprunt, E.S., Nur, A., 1979. Microcracking and healing in granites; new evidence from cathodoluminescence. Science 205, 495-497.

Srivastava, D.C., Engelder, T., 1990. Crack-propagation sequence and pore-fluid conditions during fault-bend folding in the Appalachian Valley and Ridge, central Pennsylvania. Geological Society of America Bulletin 102, 116-128.

Thorbjornsen, K.L. ,Dunne, W.M., 1997. Origin of a thrust-related fold; geometric vs kinematic tests. Journal of Structural Geology 19, 303-319.

Tarasewicz, J.P.T., Woodcock, N.H., Dickson, J.A.D., Anthony, D., 2005. Carbonate dilation breccias; examples from the damage zone to the Dent Fault, northwest England. Geological Society of America Bulletin 117, 736-745.

Twiss, R.J., Moores, E.M., 1992. Structural Geology, W.H. Freeman and Company, New York.

van der Plas, L., Tobi, A.C., 1965. A chart for judging the reliability of point counting results. American Journal of Science 263, 87-90.

van den Kerkhof, A., 1988. Phase transitions and molar volumes of CO_2-CH_4 inclusions. Bulletin de Mineralogie 111, 257-266.

Walsh, J.J., Watterson, J., Bailey, Childs, C., 1999. Fault relays, bends and branch lines. Journal of Structural Geology 21, 1019 – 1026.

Wickham, J., 1995. Fault displacement-gradient folds and the structure at Lost Hills, California (U.S.A.). Journal of Structural Geology 17, 1293-1302.

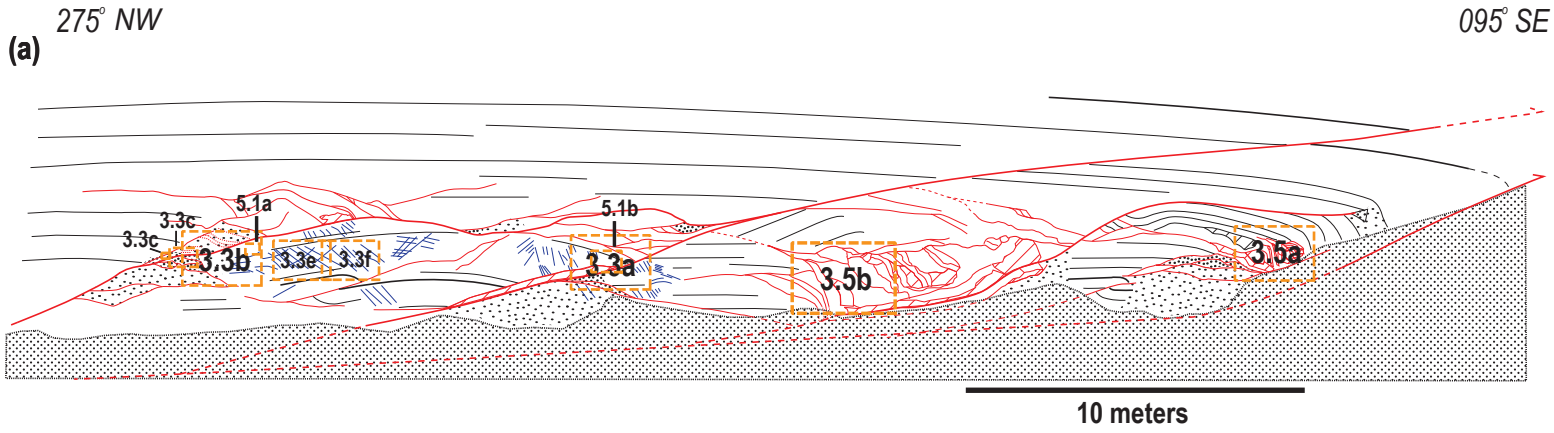
Wilson, T.H., Shumaker, R.C., 1992. Broad Top thrust sheet; an extensive blind thrust in the Central Appalachians. American Association of Petroleum Geologists Bulletin 76, 1310-1324.

Woodcock, N.H., Fischer, M., 1986. Strike-slip duplexes. Journal of Structural Geology 8, 725-735.

Worden, R.H., Oxtoby, N.H., Smalley, P.C., 1998. Can oil emplacement prevent quartz cementation in sandstones? Petroleum Geoscience 4, 129-137.

Wu, S., Groshong, R.H.,1991. Low-temperature deformation of sandstone, southern Appalachian fold-thrust belt. Geological Society of America Bulletin 103, 861-875.

APPENDICES



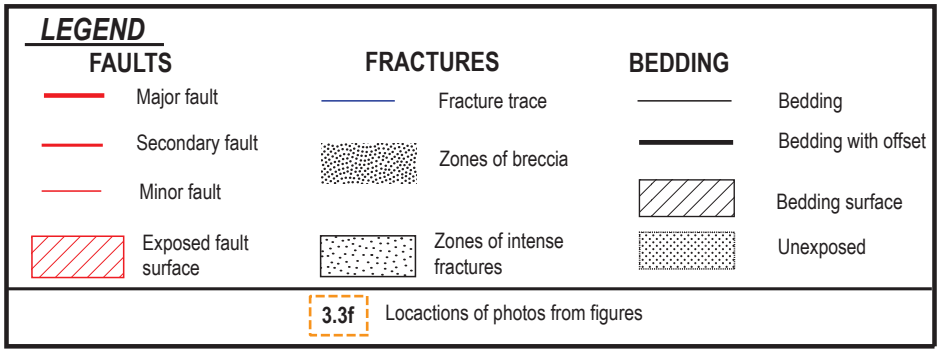


Figure A.1 - Locations of outcrop photos in Figs. 3.3, 3.5, and 5.1.



Figure A.2 - Sample locations for the chevron fold. Fold is located at 34.8893 N, 79.2434 W latitude/longitude.

Table A.1 - Fault orientation data.

STRIKE	DIP	RAKE	LOCATION
028	14 W		Fault 1B
050	38 N	84 NE	Fault 2
050	35 N		Fault 2
016	40 W		Fault 2
042	38 N		Fault 2
054	20 N		Fault 3
048	20 S	82 SW	Fault 3
052	20 N		Fault 3
048	20 N		Fault 3
020	18 W		Fault 4
052	72 S	88 SW	Minor Fault, Bedding rollover
041	30 E	80 NE	Minor fault, Bedding rollover
038	20 W	89 NE	Minor Fault
064	11 N		Minor Fault
052	10 N	60 SW	Minor Fault
042	70 E	80 SW	Minor Fault
028	59 E	75 SW	Minor Fault, Upper Rib, SE
052	79 S	84 SW	Minor Fault. Upper Rib, SE
041	21 W		Minor fault, SE Damage Zone
024	20 W		Small backthrust (Not Damage Zone)
035	16 W		Small backthrust (Not Damage Zone)

Table A.2 - Joint orientation data.

STRIKE	DIP		L (m)	S (mm)	Factor
163	70	E	0.11	5	0.022
163	70	E	0.2	70	0.003
174	67	E	0.6	20	0.030
174	67	E	0.36	20	0.018
174	67	E	0.75	10	0.075
105	69	S		100	0.000
174	16	W	0.2	20	0.010
180	70	E	1.1	100	0.011
135	25	E	0.2	10	0.020
010	40	E	0.5	20	0.025
140	40	E		150	0.000
116	89	N	0.5	50	0.010
005	2	N	**SPORADIC**		-
022	60	W	0.3	50	0.006
185	25	E	0.7	10	0.070
000	60	E	1	20	0.050
165	30	E	0.3	10	0.030
155	60	E	**SPORADIC**		-
155	43	E	2.1	20	0.105
125	48	S	0.2	40	0.005
170	65	E	**SPORADIC**		-
030	74	W	**SPORADIC**		-
045	56	E	**SPORADIC**		-
045	76	E	0.3	50	0.006
045	18	E	0.3	5	0.060
146	69	W	**SPORADIC**		-
180	39	E	**SPORADIC**		-
172	55	E	0.38	5	0.076
190	26	W	0.3	10	0.030
145	64	W	**SPORADIC**		-
050	37	N	0.5	30	0.017
060	70	N	**SPORADIC**		-
020	35	W	0.5	100	0.005
155	30	E	1	50	0.020
173	24	W	0.5	150	0.003
040	28	E	1	500	0.002
092	75	N	0.15	100	0.002
020	22	W	0.4	70	0.006
040	42	E	0.5	40	0.013
144	40	E	0.8	5	0.160
155	60	W	0.4	150	0.003
143	73	W	0.2	10	0.020
026	42	E	**SPORADIC**		-
040	80	E	**SPORADIC**		-
160	65	E	0.8	5	0.160
155	80	W	0.2	10	0.020
104	89	S	**SPORADIC**		-
140	80	W	0.5	10	0.050
105	39	S	0.7	30	0.023
156	70	W	0.15	5	0.030
131	10	S	0.1	10	0.010
165	80	W	0.3	20	0.015
153	50	E	0.4	50	0.008
165	59	W	0.4	20	0.020
110	16	N	**SPORADIC**		-
040	60	W	**SPORADIC**		-

L = **length of zone of joints**
S = **average spacing between joints**
Factor = **L / S**

Table A.3 - Damage zone bedding orientation data.

STRIKE	DIP		LOCATION
274	10	NW	NW Limb
124	10	SE	SE Limb
154	6	SE	Upper Rib SE
119	3	NW	Upper Rib NW
053	15	NW	NW Limb
064	11	NW	NW Limb
055	13	NW	NW Limb
134	4	E	Near BB-18
054	15	W	NW Limb Open Fold/Damage Zone
148	10	E	Near BB-14 and BB-15, SE Limb Open Fold
040	3	W	Above Damage Zone
080	8	NW	NW Limb above Damage Zone
034	11	W	NW Limb Open Fold/Damage Zone
050	9	N	NW Limb Open Fold/Damage Zone
110	11	N	Near BB-1
146	4	E	Near BB-18
061	4	N	Near BB-19
018	12	W	Between BB-19 and BB-20

Table A.4 - Chevron fold bedding orientation data.

STRIKE	DIP		LOCATION
034	40	N	NW Limb
048	62	S	SE Limb (CV-1)
004	14	W	Hinge, Lower Bench (CV-2)
026	50	W	NW Limb (CV-3)
009	19	W	Hinge, Upper Bench
027	63	W	Far NW Limb
129	8	SW	Hinge, Upper Bench (CV-7)
024	42	W	NW Limb (CV-9)
049	75	S	SE Limb, low
024	37	W	NW Limb, adjacent (CV-14)
049	60	S	SE Limb
028	50	W	NW Limb
056	40	S	SE Limb
030	39	W	NW Limb
036	29	E	Near Hinge Fault, SE
049	33	S	Near Hinge, Lower Bench

Table A.5 - Microstructural abundances for the chevron fold classified by primary deformation process.

		BRITTLE																CRYSTAL-PLASTIC						PRESSURE SOLUTION				NO STRUCTURE	
		Intragranular Fluid Inclusion Planes		Transgranular Fluid Inclusion Planes		Fluid Inclusions		Open Microfracture		Transgranular Microvein		Microfault		Zone of Grain Disaggregation		Cataclasite/ Healed Breccia		Deformation Lamellae		Patchy Extinction		Undulatory Extinction		Stylolite		Irregular/Sutured Grain Boundaries			
	Total Grains	%	#	%	#	%	#	%	#	%	#	%	#	%	#	%	#	%	#	%	#	%	#	%	#	%	#	%	#
Chevron Fold Samples																													
CV-1	***252***	48.0	121	2.0	5	48.8	123	1.2	3	9.9	25	0.8	2	0.0	0	8.3	21	6.0	15	3.2	8	36.5	92	4.4	11	2.4	6	8.3	21
CV-2	***253***	64.0	162	4.7	12	56.9	144	0.4	1	17.4	44	2.8	7	0.4	1	7.5	19	34.0	86	5.5	14	54.2	137	0.0	0	0.4	1	2.8	7
CV-3	***250***	46.0	115	1.2	3	17.2	43	0.0	0	7.2	18	0.8	2	0.0	0	0.0	0	3.6	9	3.2	8	25.2	63	1.6	4	6.8	17	28.0	70
CV-6	***252***	76.6	193	22.6	57	72.6	183	3.2	8	40.1	101	0.8	2	0.0	0	4.0	10	14.3	36	10.3	26	41.7	105	6.7	17	1.6	4	0.0	0
CV-7	***250***	51.2	128	2.4	6	56.4	141	0.0	0	5.2	13	0.4	1	0.0	0	1.6	4	10.0	25	5.6	14	46.0	115	1.6	4	8.8	22	6.0	15
CV-8	***250***	36.0	90	2.4	6	31.6	79	0.8	2	18.4	46	2.4	6	2.4	6	0.0	0	3.6	9	5.2	13	28.8	72	0.4	1	2.8	7	15.2	38
CV-9	***254***	42.5	108	0.8	2	67.7	172	0.0	0	4.7	12	0.0	0	0.0	0	0.4	1	20.9	53	3.9	10	47.2	120	0.0	0	0.8	2	9.4	24
CV-11	***250***	53.6	134	1.6	4	25.6	64	4.0	10	17.6	44	0.4	1	0.0	0	0.0	0	9.2	23	3.6	9	29.6	74	1.6	4	12.4	31	13.2	33
CV-12	***250***	63.6	159	7.6	19	92.4	231	2.4	6	6.8	17	0.8	2	0.0	0	0.0	0	4.8	12	6.0	15	43.2	108	0.0	0	1.2	3	1.2	3
CV-14	***250***	42.0	105	2.0	5	75.2	188	0.4	1	7.2	18	0.4	1	0.0	0	2.4	6	3.6	9	4.8	12	35.6	89	0.0	0	0.0	0	8.4	21
	Average	***52.4***	***131.5***	***4.7***	***11.9***	***54.4***	***136.8***	***1.2***	***3.1***	***13.5***	***33.8***	***1.0***	***2.4***	***0.3***	***0.7***	***2.4***	***6.1***	***11.0***	***27.7***	***5.1***	***12.9***	***38.8***	***97.5***	***1.6***	***4.1***	***3.7***	***9.3***	***9.3***	***23.2***

Table A.6 - FTIR data. Results for all individual measurements per sample.

Sample	*Number*	*Thickness (μm)*	*Corrected area*	*Water conc. Hx10^6 Si*
3F	1	130	49.3	3979.5
3F	2	130	119.5	9655.0
3F	3	130	37.9	3058.3
3F	4	130	75.6	6109.8
3F	5	130	79.5	6421.9
3F	6	130	147.9	11949.5
3F	7	130	31.9	2572.8
3F	8	130	65.1	5255.3
3F	9	130	55.4	4472.7
3F	10	130	144.0	11629.4
3F	11	130	57.9	4677.4
3F	12	130	73.3	5918.0
3F	13	130	43.9	3542.5
3F	14	130	56.8	4585.0
3F	15	130	30.7	2477.0
3F	16	130	69.2	5588.6
Average =	*5743.3*			
Max =	11949.5			
Min =	2477.0			
17B	17	120	79.4	6945.9
17B	18	120	168.2	14718.9
17B	19	120	224.6	19651.1
17B	20	120	127.8	11179.2
17B	21	120	199.4	17443.3
17B	22	120	127.9	11186.9
17B	23	120	154.1	13481.6
17B	24	120	131.4	11496.0
17B	25	120	159.8	13978.3
17B	26	120	180.0	15754.1
17B	27	120	173.2	15151.0
17B	28	120	244.2	21363.7
17B	29	120	228.2	19971.6
17B	30	120	173.6	15189.3
17B	31	120	215.3	18839.4
Average =	*15090.0*			
Max =	21363.7			
Min =	6945.9			
6V	32	185	71.8	4073.5
6V	33	185	165.1	9368.6
6V	34	185	173.3	9838.7
6V	35	185	70.3	3991.3
6V	36	185	263.8	14972.7
6V	37	185	159.1	9031.1
6V	38	185	42.6	2417.2
6V	39	185	73.3	4161.8
6V	40	185	113.9	6466.8
6V	41	185	50.1	2843.9
6V	42	185	50.8	2884.2
6V	43	185	139.4	7912.7
6V	44	185	121.8	6914.2
6V	45	185	111.7	6338.0
6V	46	185	111.9	6350.5
6V	47	185	93.4	5298.5
Average =	*6429.0*			
Max =	14972.7			
Min =	2417.2			

Table A.6 - FTIR data (cont.)

Sample	Number	Thickness (μm)	Corrected area	Water conc. $Hx10^6$ Si
10V	48	150	63.1	4417.3
10V	49	150	154.1	10786.1
10V	50	150	181.8	12722.8
10V	51	150	96.7	6770.2
10V	52	150	106.1	7423.6
10V	53	150	60.3	4224.3
10V	54	150	38.2	2676.3
10V	55	150	52.0	3637.0
10V	56	150	109.3	7647.7
10V	57	150	44.0	3078.8
10V	58	150	25.3	1767.8
10V	59	150	54.2	3790.8
10V	60	150	53.7	3756.7
10V	61	150	67.8	4744.0
10V	62	150	106.8	7477.3
10V	63	150	81.9	5733.2
Average =	*5665.9*			
Max =	12722.8			
Min =	1767.8			
11P	64	145	164.0	11878.0
11P	66	145	12.3	887.7
11P	67	145	173.0	12530.1
11P	68	145	196.9	14256.0
11P	69	145	130.9	9478.1
11P	70	145	206.0	14913.7
11P	71	145	175.2	12686.9
11P	72	145	91.4	6619.9
11P	73	145	110.3	7984.2
11P	74	145	100.9	7309.2
11P	75	145	112.9	8176.2
11P	76	145	100.3	7260.0
11P	77	145	146.4	10599.2
11P	78	145	145.7	10549.1
11P	79	145	180.2	13049.0
11P	80	145	188.0	13615.2
11P	81	145	206.8	14974.0
11P	82	145	142.6	10322.8
11P	83	145	166.3	12041.2
Average =	*10480.6*			
Max =	14974.0			
Min =	887.7			
19V	84	200	92.7	4867.5
19V	85	200	68.2	3578.0
19V	86	200	82.3	4322.3
19V	87	200	60.0	3149.0
19V	88	200	38.5	2022.3
19V	89	200	72.1	3786.4
19V	90	200	54.8	2874.9
19V	91	200	36.1	1894.9
19V	92	200	145.1	7616.6
19V	93	200	117.2	6150.7
19V	94	200	10.5	551.6
19V	95	200	53.1	2786.7
19V	96	200	66.3	3479.1
19V	97	200	55.6	2919.8
19V	98	200	71.0	3727.9
Average =	*3581.8*			
Max =	7616.6			
Min =	551.6			

Table A.6 - FTIR data (cont.)

Sample	Number	Thickness (μm)	Corrected area	Water conc. $Hx10^6$ Si
2V	99	240	114.3	4999.8
2V	100	240	99.5	4353.0
2V	101	240	55.9	2445.9
2V	102	240	211.2	9238.9
2V	103	240	63.7	2786.3
2V	104	240	35.7	1559.8
2V	105	240	84.1	3677.3
2V	107	240	134.3	5873.5
2V	108	240	104.5	4572.7
2V	109	240	48.5	2121.8
2V	110	240	113.3	4955.0
2V	111	240	34.2	1494.4
2V	112	240	63.0	2756.5
2V	113	240	19.1	836.2
2V	114	240	54.1	2366.7
2V	115	240	51.8	2267.8
Average =	*3519.1*			
Max =	9238.9			
Min =	836.2			
24V	116	125	70.9	5958.0
24V	117	125	108.4	9108.4
24V	118	125	74.9	6290.9
24V	119	125	71.0	5967.3
24V	120	125	78.4	6586.6
24V	121	125	85.6	7187.2
24V	122	125	73.9	6210.1
24V	123	125	64.8	5442.0
24V	124	125	48.1	4043.4
24V	125	125	54.2	4554.7
24V	126	125	52.1	4379.1
24V	127	125	188.6	15839.5
24V	128	125	202.4	17003.3
24V	129	125	84.0	7054.0
24V	130	125	210.2	17653.7
Average =	*8218.5*			
Max =	17653.7			
Min =	4043.4			
8V	131	130	36.0	2904.3
8V	132	130	112.8	9107.7
8V	133	130	145.6	11758.7
8V	134	130	77.2	6231.8
8V	135	130	27.6	2225.5
8V	136	130	95.2	7686.7
Average =	*6652.4*			
Max =	11758.7			
Min =	2904.3			

VITA

Jennie E. Cook was born in Richmond, VA on October 21, 1978. She graduated from high school in 1997 and attended college at Virginia Tech, where she majored in Geological Sciences. Upon graduation in 2001, she worked as a staff geologist in Pennsylvania prior to enrolling at the University of Tennessee, Knoxville in 2002 where she received a M.S. degree in Geology in 2005. She will be pursuing her doctorate degree in structural geology at the University of Wisconsin, Madison, beginning in the fall of 2005.